Report No. FRA/ORD-77-33

COMPARISON OF EXPERIMENTAL AND THEORETICAL REACTION RAIL CURRENTS, RAIL VOLTAGES, AND AIRGAP FIELDS FOR THE LINEAR INDUCTION MOTOR RESEARCH VEHICLE

David G. Elliott

JULY 1977

FINAL REPORT

Document is available to the public through the
National Technical Information Service,
Springfield, Virginia 22151

Prepared for

U. S. DEPARTMENT OF TRANSPORTATION
FEDERAL RAILROAD ADMINISTRATION
Office of Research and Development
Washington, D. C. 20590

TECHNICAL REPORT STANDARD TITLE PAGE

1. Report No. FRA/ORD-77-33	2. Government Accession No.	3. Recipient's Catalog No.
4. Title and Subtitle COMPARISON OF EXPERIMENTAL AND THEORETICAL REACTION RAIL CURRENTS, RAIL VOLTAGES, AND AIRGAP FIELDS FOR THE LINEAR INDUCTION MOTOR RESEARCH VEHICLE		5. Report Date July 1977 6. Performing Organization Code
7. Author(s) David G. Elliott		8. Performing Organization Report No. 77-36
9. Performing Organization Name and Address JET PROPULSION LABORATORY California Institute of Technology 4800 Oak Grove Drive Pasadena, California 91103		10. Work Unit No. 11. Contract or Grant No. NASA Task Order No. RD 152, Amdt. 1
12. Sponsoring Agency Name and Address Federal Railroad Administration Office of Research and Development Washington, D.C. 20590		13. Type of Report and Period Covered Final Report January 1976 - December 1976 14. Sponsoring Agency Code

15. Supplementary Notes

16. Abstract

Measurements of reaction rail currents, reaction rail voltages, and airgap magnetic fields in tests of the Linear Induction Motor Research Vehicle (LIMRV) were compared with theoretical calculations from the mesh/matrix theory. It was found that the rail currents and magnetic fields predicted by the theory are within 20 percent of the measured currents and fields at most motor locations in most of the runs, but differ by as much as a factor of two in some cases. The most consistent difference is a higher experimental than theoretical magnetic field near the entrance of the motor and a lower experimental than theoretical magnetic field near the exit. The observed differences between the theoretical and experimental magnetic fields and currents do not account for the differences of as much as 26 percent between the theoretical and experimental thrusts.

17. Key Words (Selected by Author(s))	18. Distribution Statement
Linear induction motors, Linear electric motors, High-speed ground transportation	Document is available to the public through the National Technical Information Service, Springfield, VA 22151

19. Security Classif. (of this report)	20. Security Classif. (of this page)	21. No. of Pages	22. Price
UNCLASSIFIED	UNCLASSIFIED		

NOTICE

This document is disseminated under sponsorship of the Department of Transportation in the interest of information exchange. The United States Government assumes no liability for its contents or use thereof.

The contents of this report reflect the views of the Jet Propulsion Laboratory, which is responsible for the facts and the accuracy of the data presented herein. The contents do not necessarily reflect the official views or policy of the Department of Transportation. This report does not constitute a standard, specification, or regulation.

The United States Government does not endorse products or manufacturers. Trade or manufacturers' names appear herein solely because they are considered essential to the object of this report.

PREFACE

The work described in this report was performed by the Propulsion Division of the Jet Propulsion Laboratory for the National Aeronautics and Space Administration under Contract NAS 7-100.

ACKNOWLEDGEMENTS

Valuable assistance was provided by R. B. Powell, AiResearch Manufacturing Company, in supplying additional details of the experiments and in furnishing enlarged photographic prints of the oscillograph records. Dr. John Stickler of Transportation Systems Center, Cambridge, Mass., reviewed the manuscript and made numerous useful suggestions.

CONTENTS

CONTENTS (contd)

TABLES

FIGURES

IGURES (contd)

FIGURES (contd)

FIGURES (contd)

FIGURES (contd)

I. INTRODUCTION

Linear induction motor tests in the past have concentrated on measurement of overall forces and powers. In a few cases search coils have provided magnetic field measurements at discrete points.

Such tests have permitted only partial comparison between experiment and theory. Theory predicts complex variations of secondary (reaction rail) current and airgap magnetic field both longitudinally (in the direction of motion) and transversely (at right angles to the direction of motion in the plane of the gap). Comparison with these predictions requires measurements of rail current and magnetic field at a resolution of about a slot pitch in the longitudinal direction and of about one fourth of the motor width in the transverse direction.

A measurement system for current and field distribution was developed by AiResearch Manufacturing Company and used in tests of the Linear Induction Motor Research Vehicle (LIMRV) at speeds up to 65 m/s[1] and later in tests at speeds to 89 m/s.[2]

The measurement system consists of current sensors and field search coils attached to the reaction rail at several transverse locations. As the vehicle passes, continuous curves of rail current, magnetic field, and also sidebar voltage are recorded. Longitudinal resolution is set by the size of the sensors at about one slot pitch. Transverse resolution is set by sensor spacing at one fourth of the motor width.

---

(1) D'Sena, G. O., and McConville, J. H., LIM Research Vehicle Reaction Rail Current Distribution Tests, Report No. FRA-OR&D-75-18, Federal Railroad Administration, Washington, D. C., Sept. 1973.

(2) Powell, R. B., and McConville, J. H., Linear Induction Motor Research Vehicle Reaction Rail Current and Airgap Flux Distribution Test, AiResearch Document No. 75-11965, Federal Railroad Administration, Washington, D. C., Nov. 1975.

II. LIMRV TEST RUNS

Seven LIMRV runs are reported in Reference 2: Runs 539 through 545. Runs 539 and 540 are at nearly the same conditions, and Run 540 is chosen for analysis here. Runs 542 and 544 are also nearly at the same conditions, and Run 544 is chosen for analysis here.

A. Operating Conditions

The five runs chosen for analysis are shown on a plot of thrust versus slip frequency at constant current in Figure 1. There are two medium-speed (40 m/s) runs: Run 540 at a slip frequency of 16 Hz and Run 544 at a slip frequency of 107 Hz. Run 540 is at a slip frequency near the value for peak thrust and peak power factor and represents normal cruising conditions for an operational vehicle. Run 544 is at a high slip that might be encountered during acceleration if fixed frequency is used.

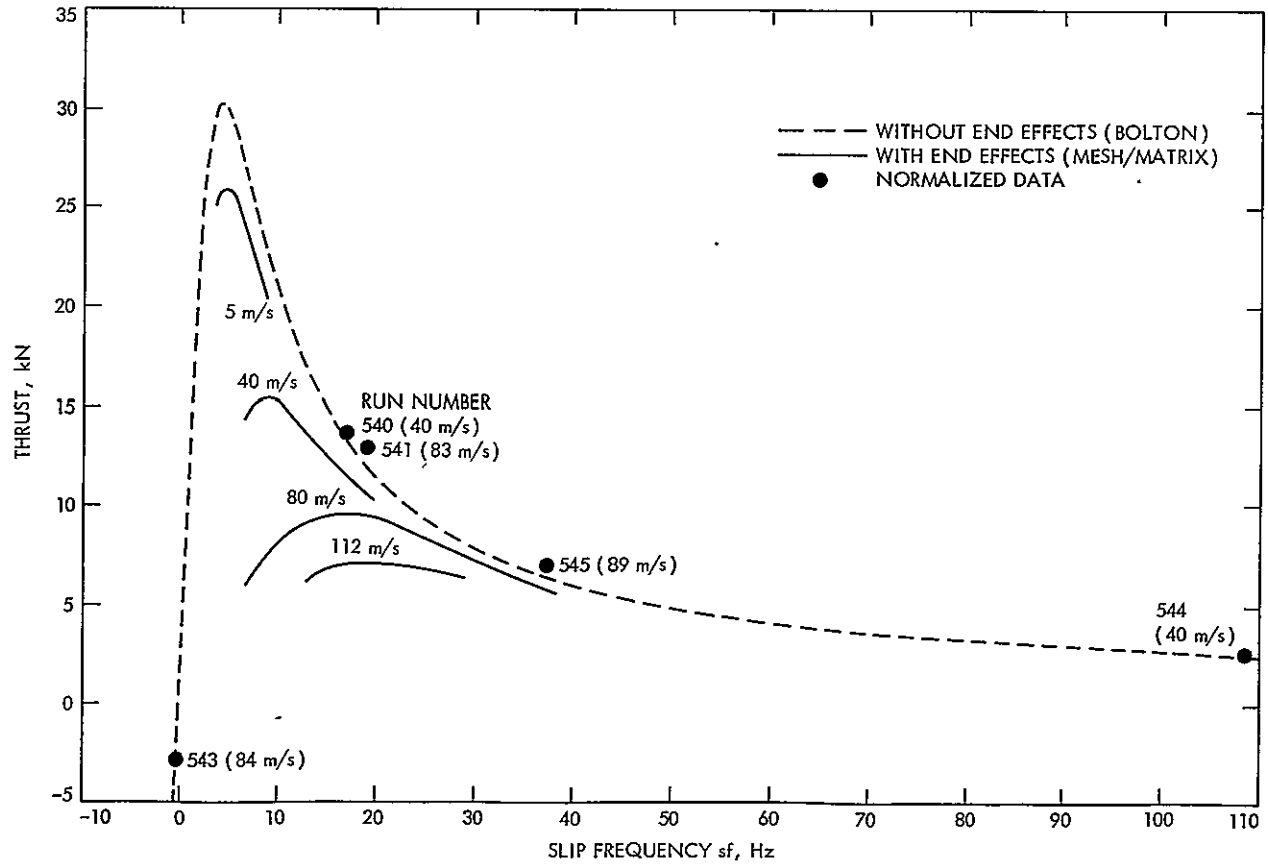

Figure 1. Theoretical thrust of LIMRV at 38.1-mm gap and 2000 A compared with measured thrusts normalized to 2000 A

There are three high-speed (83-89 m/s) runs: Runs 541, 543, and 545 at slip frequencies of 19, -1, and 37 Hz, respectively. Run 541 represents normal cruising operation. Run 545 represents moderately high-slip operation. Run 543 is at essentially zero slip but slightly on the power-generating, or braking side of zero slip.

The operating conditions for the five runs are summarized in Table 1.

Table 1. LIMRV operating conditions[a]

Run No.	Speed, m/s	Frequency, Hz	Current, A	Voltage, V	Power factor	Slip	Slip frequency, Hz
540	39.79	72.4	2181	208.1	0.686	0.227	16.4
541	82.97	135.3	1903	329.1	0.650	0.137	18.6
543	83.78	117.0	1637	404.1	0	-0.007	-0.8
544	39.83	162.8	2278	250.1	0.331	0.656	106.8
545	89.32	162.4	2350	342.3	0.542	0.226	36.8

[a]Speed, frequency, current, voltage, and power factor from Table 3-1 of Reference 2. Slip and slip frequency calculated from speed and frequency using pole pitch of 355.47 mm.

B. Comparison of Theoretical and Experimental Thrusts and Powers

Figure 1 also presents curves of theoretical thrust for comparison with the measurements. The theoretical curves are calculated for 2000-A phase current, and the measured thrusts are normalized to the same current by multiplying the measured thrusts by the square of the ratios of 2000 A to the actual current. The LIMRV motor constants used in the theoretical calculations are summarized in Table 2.

Table 2. LIMRV motor constants

Primary			
length	L	3810	mm
width	c	254	mm
gap	g	38.1	mm
number of slots	M	160	
number of slots per pole	N_{spp}	15	
slot pitch	τ_s	23.698	mm
slot width	w	16.0	mm
winding resistance	R_1	$6(1+3\times10^{-5}f^2)$	mΩ/phase
Secondary (rail)			
effective thickness	h	7.07	mm
conductivity	σ	27.6	MS/m
upper sidebar width	c_{e_1}	98.6	mm
lower sidebar width	c_{e_2}	192.0	mm

The dashed curve in Figure 1 gives the thrust for a sheet-rotor induction motor without end effects calculated from Bolton's theory.[3,4] The gap used is the Table 2 value multiplied by the Carter factor of 1.15 to account for the slots. The length used is the Table 2 length of 3.81 m reduced by a factor to account for the effect of the reduced current in the single-layer regions at each end of the motor. The reduced current is assumed to reduce the thrust in the single-layer regions in proportion to current squared. The single-layer winding extends over 10 slots at each end of the motor and the double-layer

[3] Bolton, H., "Transverse Edge Effect in Sheet-Rotor Induction Motors," Proc. IEE, Vol. 116, No. 5, pp. 725-731, May 1969.

[4] Bolton, H., "Forces in Induction Motors with Laterally Asymmetric Secondaries," Proc. IEE, Vol. 117, No. 12, pp. 2241-2248, Dec. 1970.

winding extends over 140 slots in the middle. The current in the double-layer slots is 1.732 times the current in the single-layer slots, and, therefore, the effective length is taken to be

$$L_{eff} = 3.81\frac{\frac{20}{1.732^2} + 140}{160} = 3.49 \text{ m}$$

Figure 1 shows that the measured LIMRV thrusts, normalized to 2000 A, are equal to or slightly higher than the Bolton thrust. Thus, the LIMRV thrust is surprisingly high, equal to the thrust that would be expected without end losses. A possible explanation for the high measured thrust is that the effective width of the LIMRV motor is greater than the physical width due to fringing of the magnetic field at the sides, the thrust added at the sides compensating for the loss due to end effects. This point is discussed further in Section VII (p. 42).

The thrust predictions of the mesh/matrix theory[5] for speeds of 5, 40, 80, and 112 m/s are also shown in Figure 1. As the speed increases from 5 to 112 m/s, the peak thrusts predicted by the mesh/matrix theory decrease by a factor of three, and the slip frequencies for peak thrust increase from 5 to 17 Hz. The thrusts predicted by the mesh/matrix theory are 18 to 26 percent below the measured thrusts.

The thrust comparisons are given again in Table 3 for the actual run currents, together with comparisons of the input powers and reactive powers. The theoretical input powers are below the measured values by about the same amount as the thrust. The theoretical and experimental reactive powers, however, agree within 9 percent.

(5) Elliott, D. G., Matrix Analysis of Linear Induction Machines, Report No. FRA-OR&D-75-77, Federal Railroad Administration, Washington, D. C., Sept. 1975.

Table 3. Comparison between experimental and theoretical (mesh/matrix) thrusts and powers

Run No.	Thrust, kN			Input power, kW			Reactive power, kVAR		
	Exp.[a]	Theo.	$\frac{\text{Theo.}}{\text{Exp.}}$	Exp.[b]	Theo.	$\frac{\text{Theo.}}{\text{Exp.}}$	Exp.[b]	Theo.	$\frac{\text{Theo.}}{\text{Exp.}}$
540	16.30	13.33	0.82	934	807	0.86	991	979	0.99
541	11.77	8.76	0.74	1221	970	0.79	1428	1466	1.03
543	-1.92	-1.83	0.95	0	69	—	1985	1648	0.83
544	3.34	2.67	0.80	566	487	0.86	1613	1762	1.09
545	9.73	7.91	0.81	1308	1112	0.85	2028	2101	1.04

[a] From Table 3-1 of Reference 2.

[b] From currents, voltages, and power factors in Table 3-1 of Reference 2.

III. MEASUREMENTS OF RAIL CURRENT, MAGNETIC FIELD, AND SIDEBAR VOLTAGE

A. Method of Measurement

The experimental arrangement is shown in Figure 2. Three current sensors, two field sensors, and one pair of sidebar voltage contacts are located on a vertical line at the first sensor station encountered by the motor. Two current sensors, one field sensor, and another pair of sidebar voltage contacts are located on a vertical line at a second station a half pole pitch farther along.

The current sensors consist of coils with axes in the longitudinal (x) direction so as to respond to the magnetic field in the x-direction produced by rail currents in the vertical or transverse (z) direction. The magnetic field sensors consist of coils with axes in the y-direction, perpendicular to the gap. The current sensors and field coils are counted in pairs, one on each side of the rail, connected in series. Twisted leads are brought out to the data system. The output voltages of the current sensor coils and field coils are electronically integrated before recording so that the signal fed to the oscillograph is proportional to the instantaneous magnetic flux.

The sidebar voltage contacts are connected to the data system through leads located as far outside the fringing field of the sides of the motor as possible, and extending 12 m in either direction so that the leads are not brought together until they are well outside the fringing field at the ends of the motor.

B. Experimental Oscillograph Records

The recordings of current sensor flux, magnetic field coil flux, and sidebar voltage are presented as oscillograph records in Reference 2. In general appearance, the records present a stretched-out view of the current, field, and sidebar voltage waveforms. The traveling waves of those quantities move relative to the rail at a speed equal to the synchronous speed times the slip. Therefore, only a fraction (equal to the slip) of the full number of poles of the waveform is recorded. In the particular case of zero slip (closely approached by Run 543) the waves are stationary relative to the rail, and the oscillograph recordings show no oscillation of the quantity, only the rise and fall at the entrance and exit.

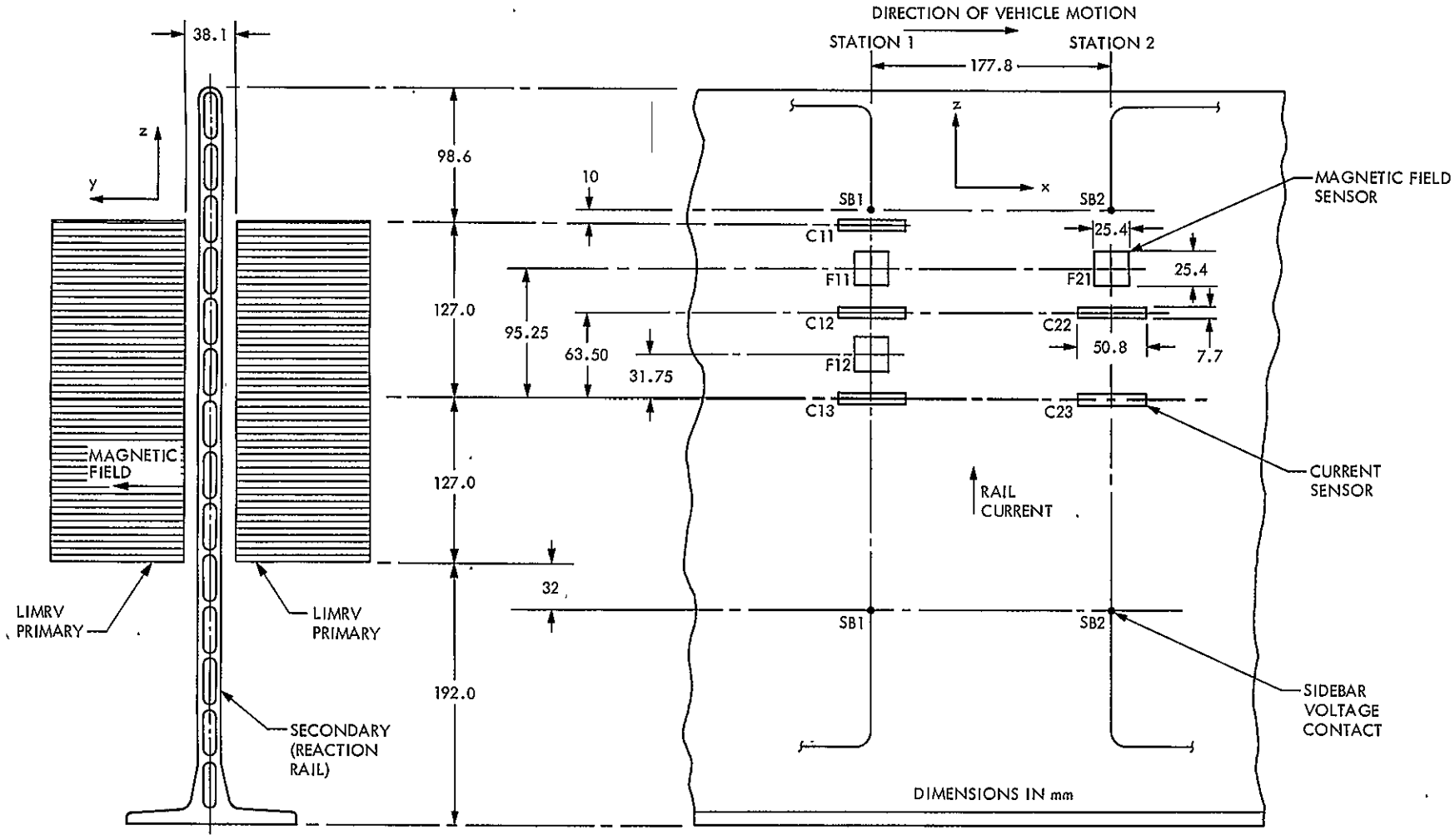

Figure 2. Arrangement of current, magnetic field, and sidebar voltage sensors for LIMRV tests

The oscillograph records at the second sensor station show waves shifted backward (to the left in Figure 2) since the waves travel to the left and the second sensor station is encountered at a later time. (One oscillograph channel in Reference 2, that for field sensor F21, has reversed polarity from the others and shows the correct behavior when inverted.)

IV. THEORETICAL RAIL CURRENT, MAGNETIC FIELD, AND SIDEBAR VOLTAGE

The longitudinal distributions of rail current, magnetic field, and sidebar voltage are calculated from the mesh/matrix theory (Reference 5), and the transverse distributions of current and field are calculated from Bolton's theory (References 3 and 4).

A. Calculation of Longitudinal Distributions

The mesh/matrix theory gives values of rail current I2(k) and gap field B(k) at closely spaced mesh points k along the longitudinal (x) direction. The theory assumes the reaction rail to be slotted in the transverse (z) direction inside the motor so that longitudinal (x-directed) currents flow only in the sidebars. The currents I2(k) are thus the constant transverse currents per mesh spacing, and the fields B(k) are the constant magnetic fields over each mesh.

B. Calculation of Transverse Distributions

In the actual induction motor with a continuous, unslotted reaction rail the transverse current decreases toward the edges of the motor as more and more of the current turns and flows longitudinally. At the same time the magnetic field increases toward the edges because there is less secondary current to oppose the field of the primary. The transverse distributions of current and field can be calculated from Bolton's theory (References 3 and 4).

C. Combined Longitudinal and Transverse Distributions

Calculations can be made for a rotating slotted-rotor motor, using the equations of Reference 5, Section X, to find the constant values of transverse current and magnetic field that give the same terminal conditions (same real and reactive powers) as given by Bolton's theory for a sheet rotor. The slotted-rotor current can be defined as the mean current of the sheet-rotor motor, and the slotted-rotor field can be defined as the mean field. (Neither mean value is exactly the same as the average over the Bolton current or field distribution.) The transverse distributions of current and field can then be expressed as ratios of local current to mean current and local field to mean

field. Since the mesh/matrix theory assumes a slotted rail, it is logical to multiply the individual mesh currents and fields by the ratios of the Bolton values to the slotted-rotor values to arrive at the predicted transverse distributions for each mesh. This is the approach used here to arrive at the combined longitudinal and transverse distributions.

D. Theoretical Transverse Distributions for the LIMRV Runs

1. Run 541. Figure 3 shows the theoretical transverse distributions of rail current amplitude and magnetic field amplitude calculated from Bolton's theory (Reference 4) for the conditions of Run 541, the high-speed, low-slip, peak-thrust run. The distributions are presented as ratios of local amplitude to mean amplitude, the mean amplitudes being the constant amplitudes in the slotted-rotor motor of equal terminal conditions.

Figure 3 shows that the transverse current amplitude is maximum near the center of the motor (slightly off center because of the rail asymmetry) and decreases to zero at the edges of the rail as more and more of the current turns and flows longitudinally. The magnetic field is minimum near the center, reaches a maximum at each edge of the motor, and drops (by the assumptions

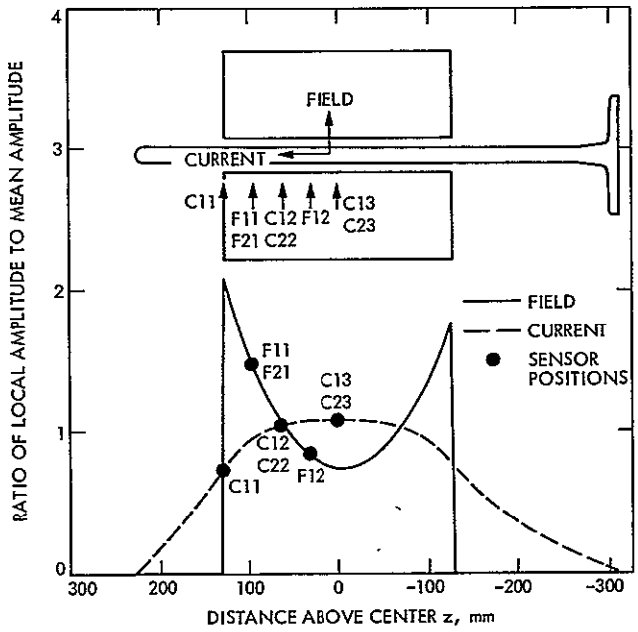

Figure 3. Theoretical (Bolton) transverse amplitude ratios for Run 541 (low-slip, peak-thrust)

of Bolton's theory) to zero outside. In an actual motor, the peaks in the field are not as sharp as shown since there is fringing field outside the motor.

The theoretical phase shifts of the current and field in Run 541 are shown in Figure 4. The phase shifts are given relative to the mean phase angles, which are the constant phase angles for the slotted-rotor motor. The current phase angle increases from a minimum near the center to a maximum in the sidebars. The field phase angle undergoes a similar, but larger, shift.

The positions of the current and field sensors in the LIMRV tests are shown on the outline of the motor and rail at the top of Figure 3. The sensor positions are also marked on the curves.

2. Run 543. Figures 5 and 6 show the amplitude ratios and phase shifts, respectively, for Run 543, the run at near-zero slip. The distribution of current amplitude is similar to that in Run 541, but the magnetic field is almost flat. The phase shifts are reversed compared with Run 541 because of the negative slip, and they have a smaller variation.

3. Run 545. The distributions for Run 545, the medium-slip, high-speed run, are shown in Figures 7 and 8. The distributions are similar to those for the lower-slip Run 541 except that there is an additional local peak in the field phase near the center of the motor.

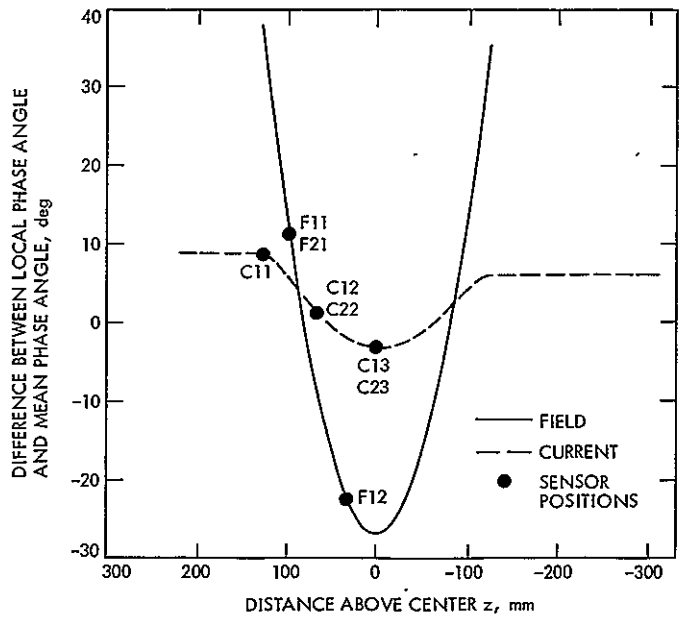

Figure 4. Theoretical (Bolton) transverse phase shifts for Run 541 (low-slip, peak-thrust)

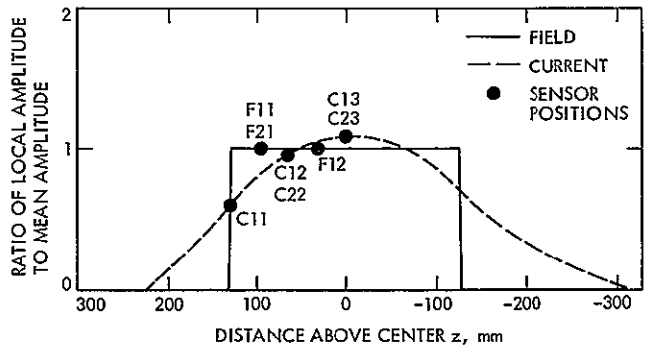

Figure 5. Theoretical transverse amplitude ratios for Run 543 (zero-slip)

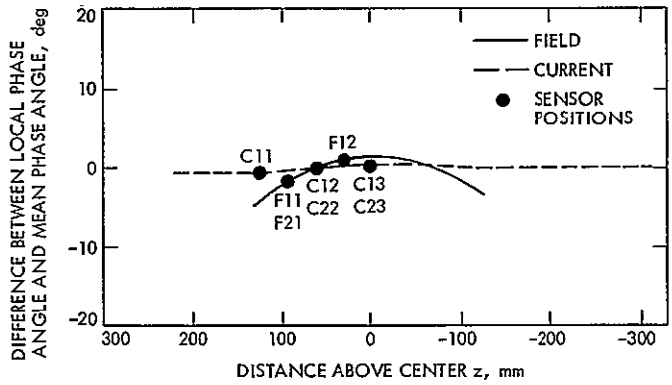

Figure 6. Theoretical transverse phase shifts for Run 543 (zero-slip)

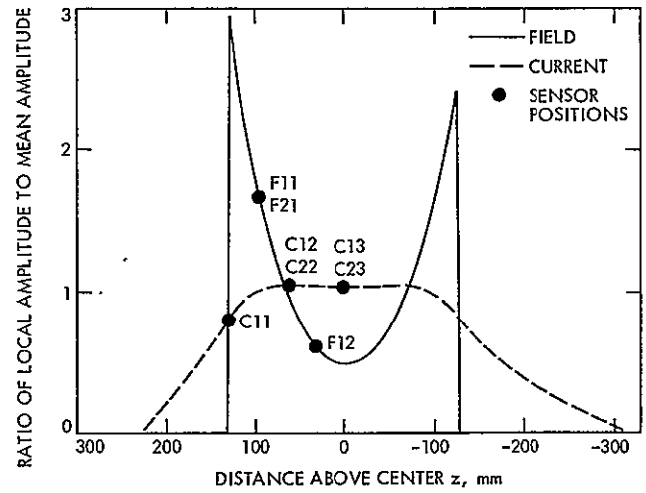

Figure 7. Theoretical transverse amplitude ratios for Run 545 (medium-slip)

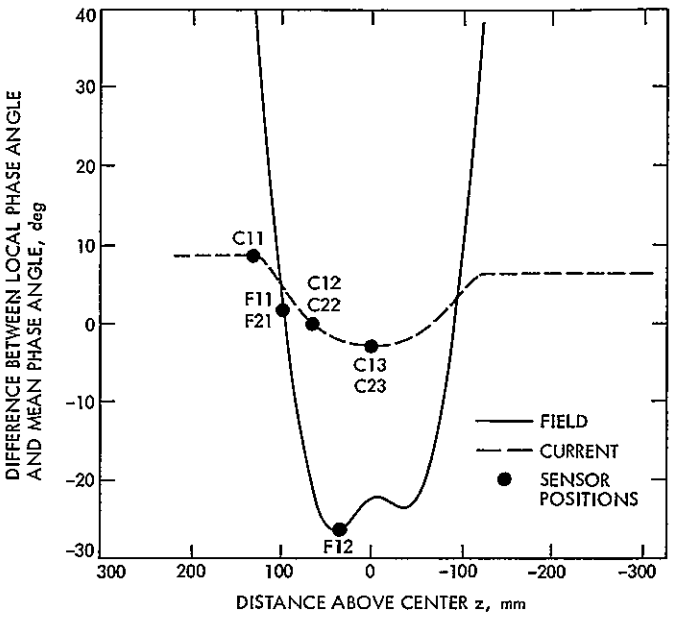

Figure 8. Theoretical transverse phase shifts for Run 545 (medium-slip)

4. Run 540. The distributions for the medium-speed, low-slip Run 540, shown in Figures 9 and 10, are essentially the same as those for the higher-speed Run 541.

5. Run 544. The largest transverse variations occur in high-slip Run 544 as shown in Figures 11 and 12. The magnetic field at the edge is ten times the field at the center, and the field phase shift goes from zero at the center to a negative 40 deg halfway to the edge and to a positive 40 deg at the edge.

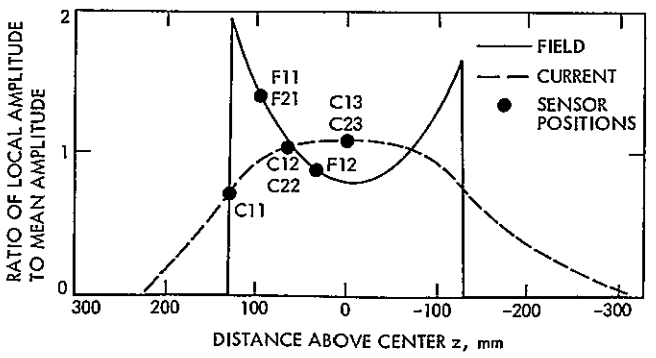

Figure 9. Theoretical transverse amplitude ratios for Run 540 (low-slip, peak-thrust)

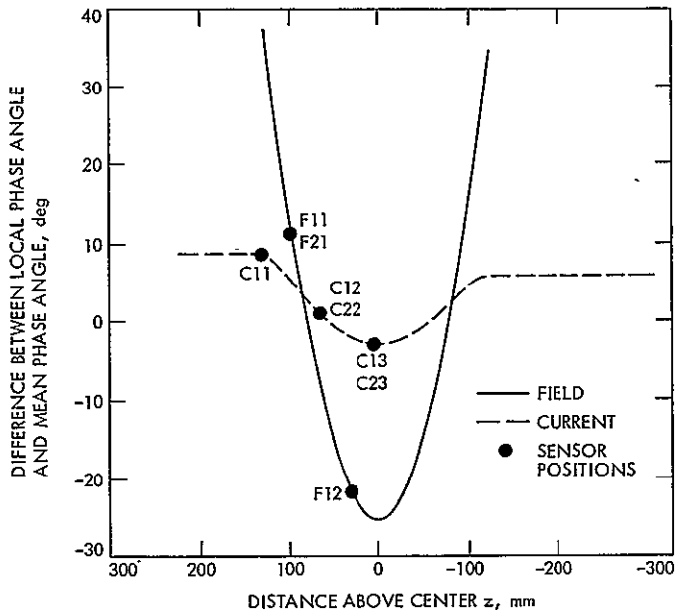

Figure 10. Theoretical transverse phase shifts for Run 540 (low-slip, peak-thrust)

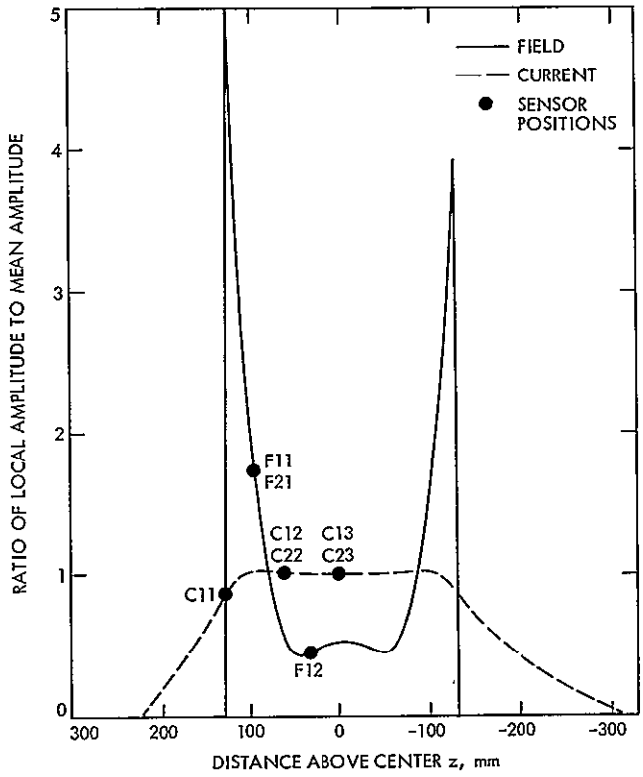

Figure 11. Theoretical transverse amplitude ratios for Run 544 (high-slip)

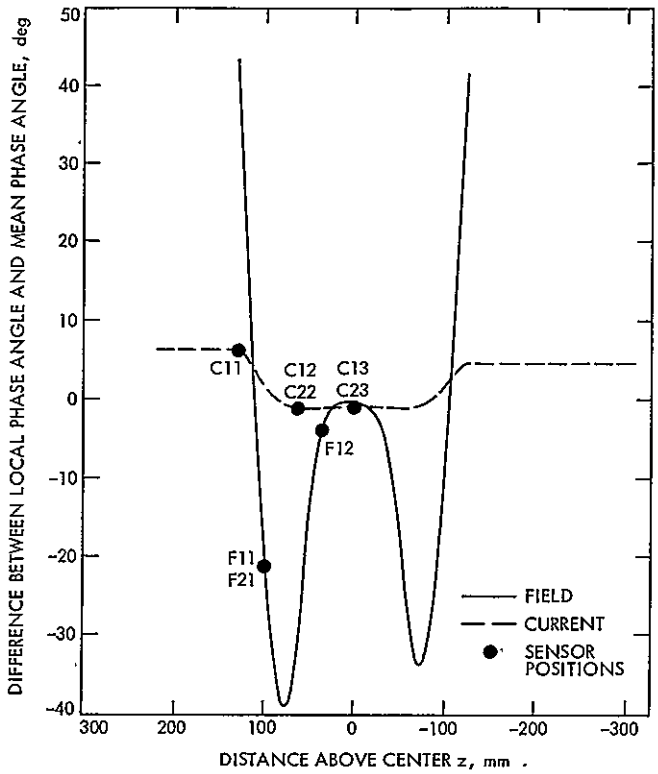

Figure 12. Theoretical transverse phase shifts for Run 544 (high-slip)

The amplitude ratios and phase shifts at the sensor positions for each of the five runs are given numerically in Table 4. Those amplitude ratios and phase shifts are the ones to be applied to the currents and fields from the mesh/matrix program to obtain the theoretical currents and fields at the z-coordinate of each sensor.

E. Theoretical Longitudinal Distributions for the LIMRV Runs

1. Run 541. Figure 13 presents the theoretical amplitude of the rail current at the position of current sensor C12 in Run 541 as a function of longitudinal distance x. The direction of motion of the rail relative to the motor is from left to right. The curve in Figure 13 is a plot of the rail current amplitude from the mesh/matrix theory, multiplied by the factor 1.036 from Table 4 to account for the transverse position (height) of sensor C12. The current is plotted as amperes in the z-direction per millimeter in the x-direction and is the peak, not rms, amplitude. The current shows two reduced-amplitude phase

Table 4. Bolton field and current factors at sensor positions

Sensor	C11		C12, C22		C13, C23		F11, F21		F12	
Type	Current		Current		Current		Field		Field	
Height, mm	127.0		63.5		0.0		95.25		31.75	
Run No.	Amplitude ratio	Phase shift, deg	Amplitude ratio	Phase shift, deg	Amplitude ratio	Phase shift, deg	Amplitude ratio	Phase shift, deg	Amplitude ratio	Phase shift, deg
540	0.714	9	1.034	1	1.085	-3	1.418	11	0.883	-22
541	0.725	9	1.036	1	1.077	-3	1.465	11	0.849	-23
543	0.611	-1	0.962	0	1.081	0	1.003	-2	1.000	1
544	0.865	6	1.013	-1	1.001	-1	1.667	-22	0.468	-4
545	0.787	8	1.039	0	1.026	-3	1.683	2	0.618	-27

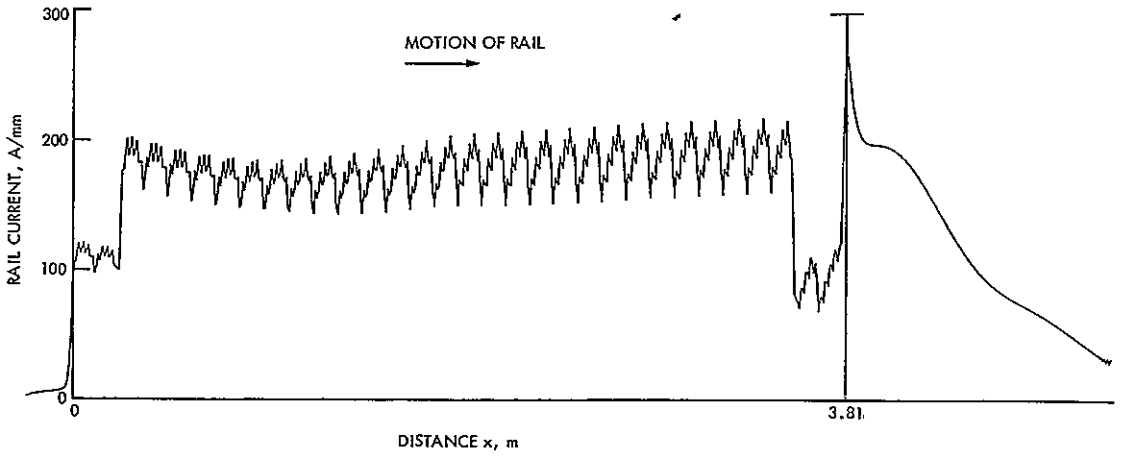

Figure 13. Theoretical amplitude of rail current at sensor C12 height in Run 541

belts at each end, corresponding to the single-layer slots, and 28 full-amplitude phase belts between. Within each phase belt, five smaller peaks are visible, corresponding to the individual slots. The current decays slowly beyond the exit of the motor after reaching a sharp peak immediately at the exit.

Figure 14 presents the theoretical amplitude of the magnetic field at the position of field sensor F11 in Run 541, as a function of distance. The curve is a plot of the magnetic field amplitude from the mesh/matrix theory multiplied by the factor 1.465 from Table 4 to account for the transverse position of sensor F11. The field shows the slow rise characteristic of linear induction motor operation at high speed. The 32 phase belts are visible as steps. The decay of the magnetic field beyond the exit has a time constant similar to that of the current.

The reason for the choice of 166 mT (millitesla) as the first scale coordinate for the field in Figure 14 is that this field gives one major unit of deflection on the oscillograph record.

The theoretical amplitude of the sidebar voltage in Run 541, calculated from the mesh/matrix theory, is plotted as a function of distance in Figure 15. The sidebar voltage varies between 0.1 and 0.3 V, with a distance between peaks of two pole pitches. (The 0.465-V scale coordinate is the value for one major unit of deflection on the oscillograph.)

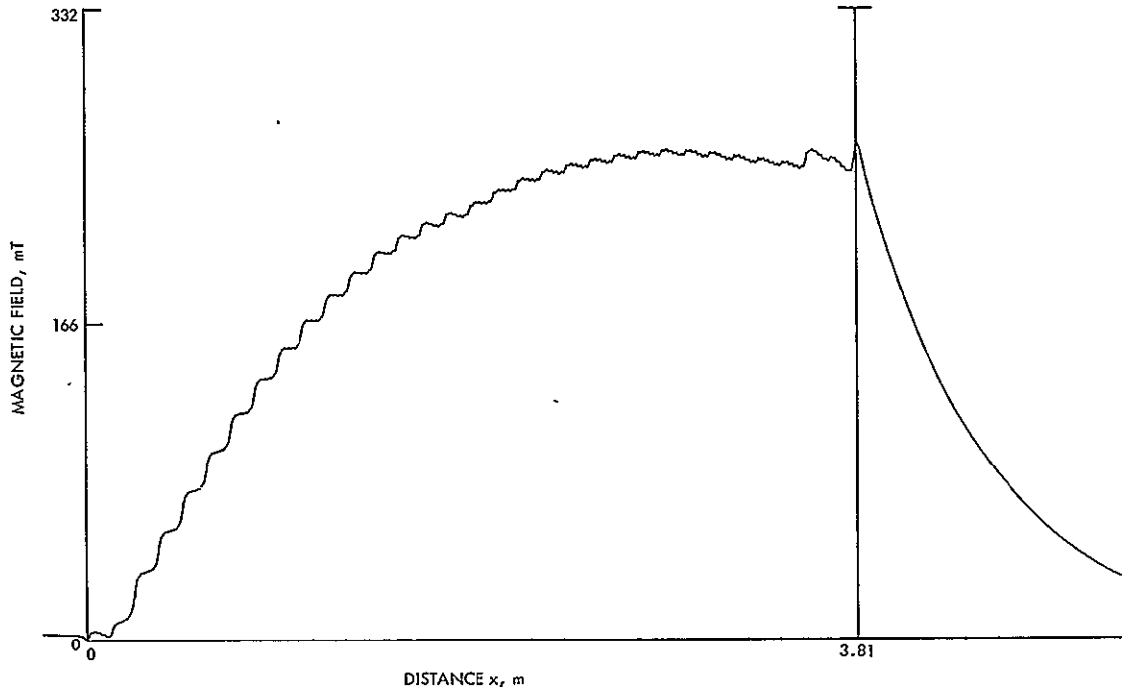

Figure 14. Theoretical amplitude of magnetic field at sensor F11 height in Run 541

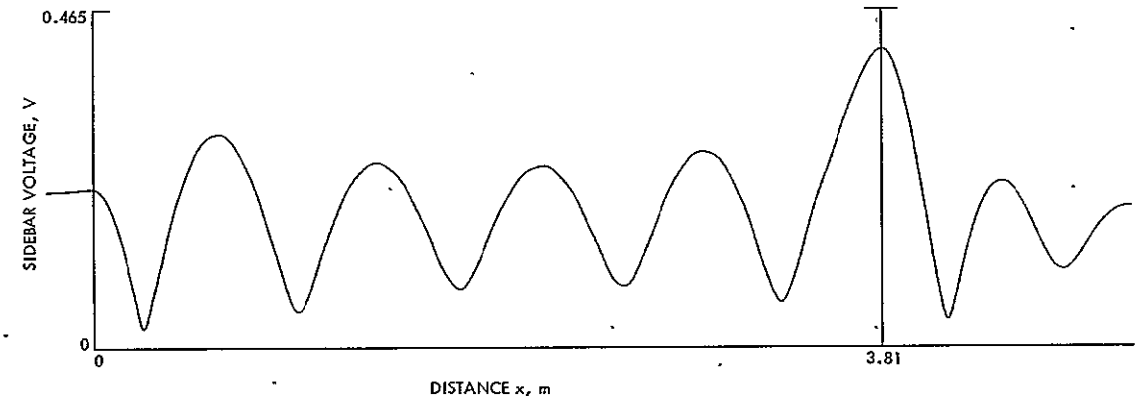

Figure 15. Theoretical amplitude of sidebar voltage in Run 541

2. Run 543. The theoretical longitudinal distribution of rail current for Run 543, the run at near-zero slip, is shown in Figure 16. The current decreases steadily throughout the double-layer region and has a peak at the exit equal to three times the maximum value inside the motor. The current does not drop back to the peak interior value until a distance is reached a third of the motor length beyond the exit.

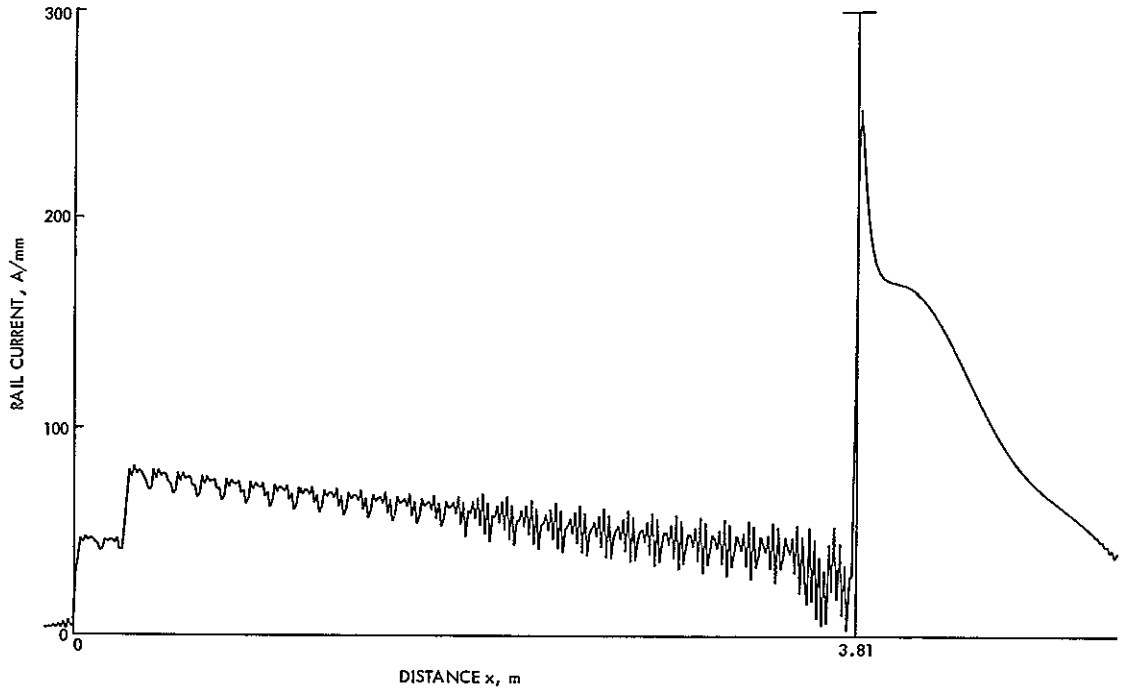

Figure 16. Theoretical amplitude of rail current at sensor C12 height in Run 543

The theoretical magnetic field amplitude in Run 543 is plotted in Figure 17. The field rises linearly from the entrance to the exit and never reaches a constant value. The sidebar voltage is shown in Figure 18.

3. Run 545. The theoretical longitudinal distributions of current and magnetic field in Run 545, the medium-slip, high-speed run, are shown in Figures 19 and 20, respectively. The motor appears to operate in two halves; the magnetic field (Figure 20) rises and falls in the first half and rises and falls again in the second half. The current (Figure 19) has a saddle shape in each half, and the current reaches a peak at the center. There is also an abrupt increase in slot harmonic amplitude at the center. (The resolution of the data was not sufficient to show if this occurred in the actual motor.) The sidebar voltage is not plotted because the oscillograph record of sidebar voltage for Run 545 was not clear enough for comparison.

4. Run 540. The longitudinal distributions for Run 540, the medium-speed, low-slip run, are shown in Figures 21-23. The curves are similar in shape to those for Run 545, with two repeated patterns of current and field. The sidebar voltage, however (Figure 23), shows a steady decay in oscillation amplitude from entrance to exit.

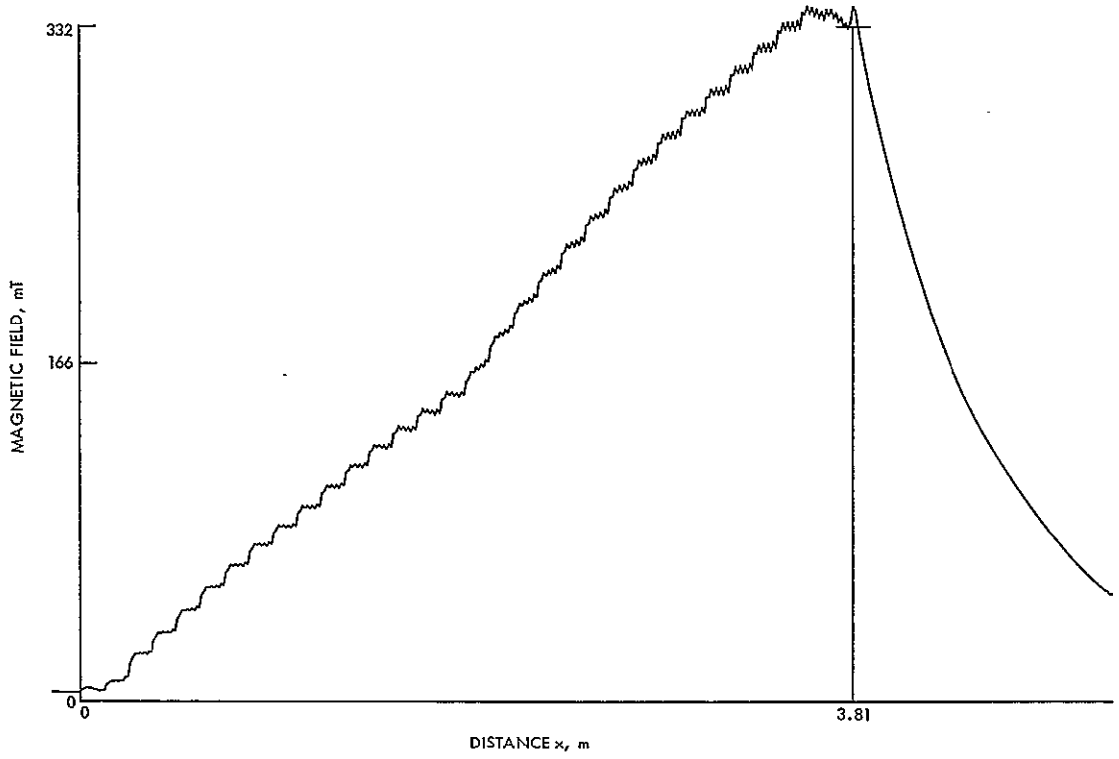

Figure 17. Theoretical amplitude of magnetic field at sensor F11 height in Run 543

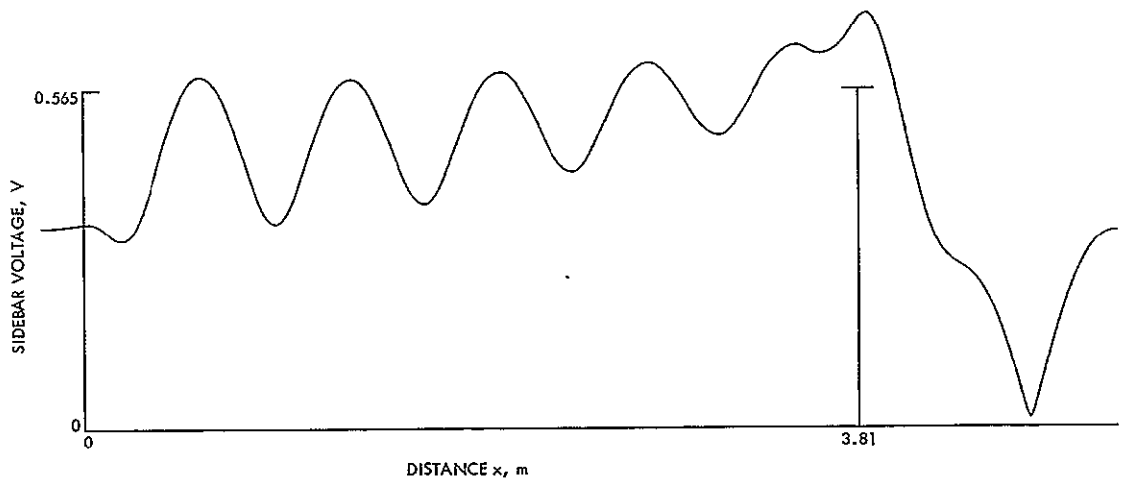

Figure 18. Theoretical amplitude of sidebar voltage in Run 543

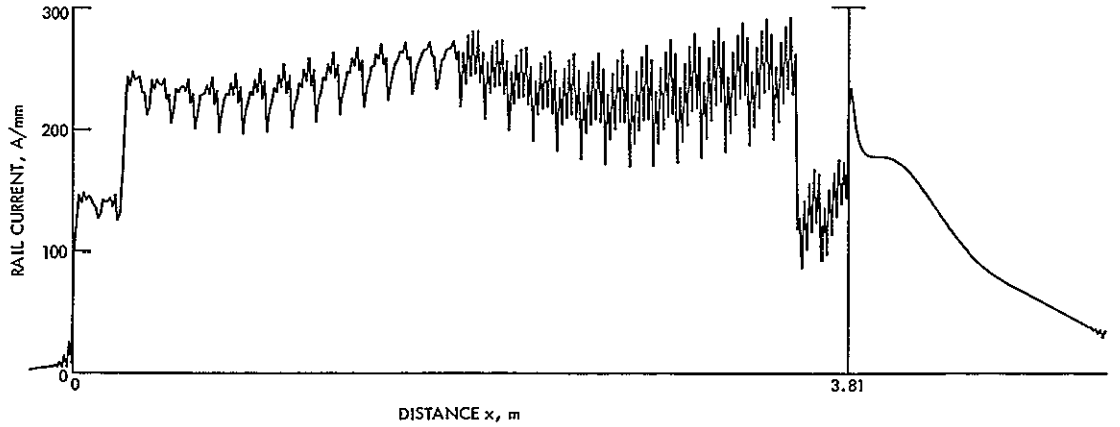

Figure 19. Theoretical amplitude of rail current at sensor C12 height in Run 545

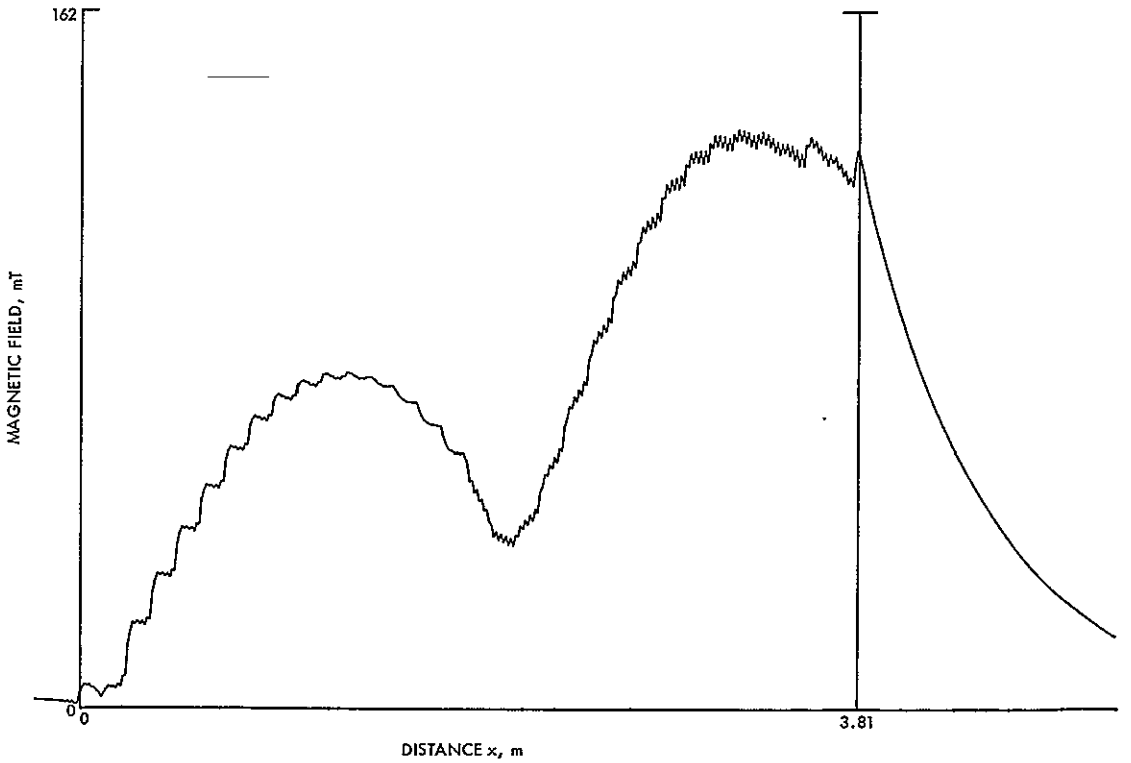

Figure 20. Theoretical amplitude of magnetic field at sensor F11 height in Run 545

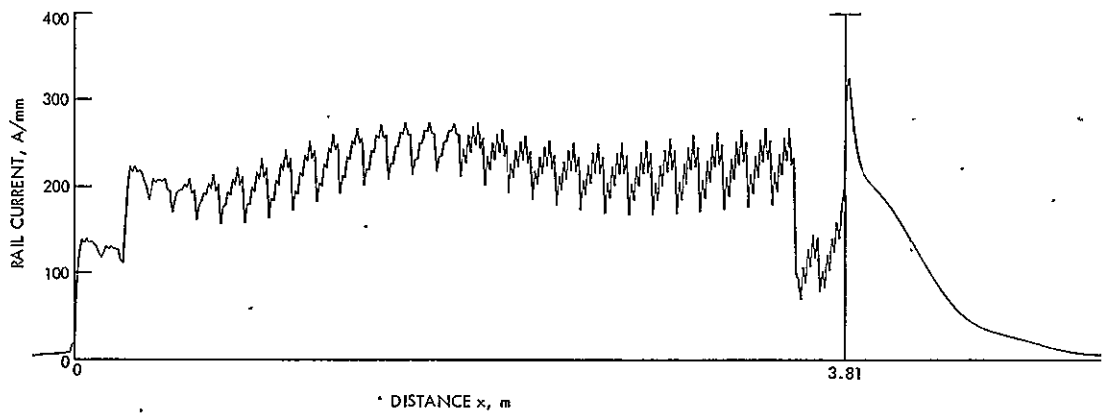

'igure 21. Theoretical amplitude of rail current at sensor C13 height in Run 540

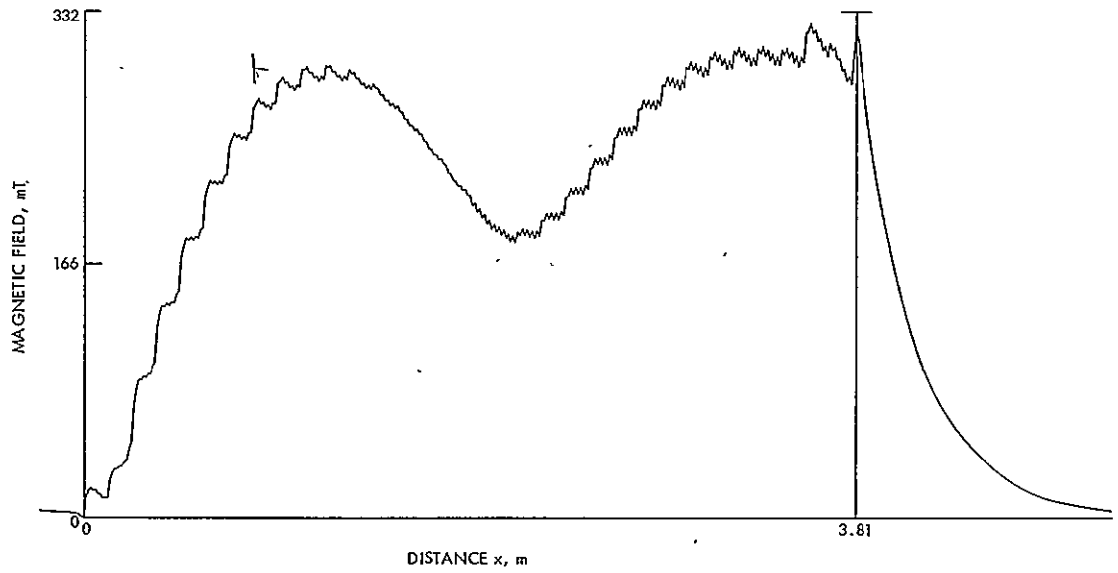

Figure 22. Theoretical amplitude of magnetic field at sensor F11 height in Run 540

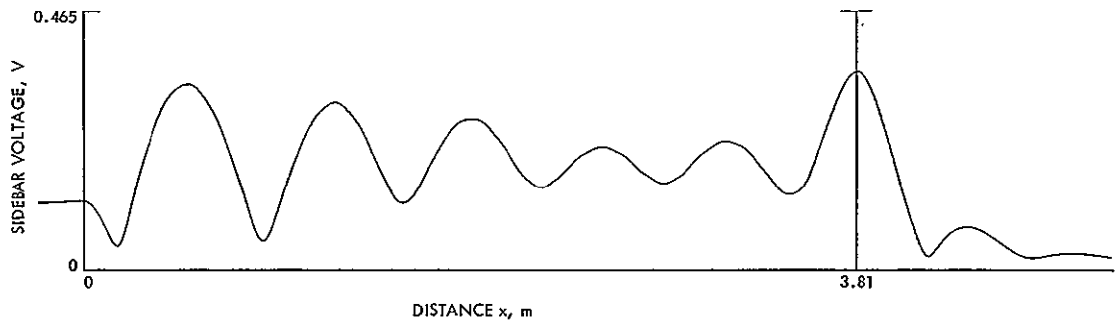

Figure 23. Theoretical amplitude of sidebar voltage in Run 540

5. Run 544. The flattest longitudinal distributions occur for the high-slip Run 544. The current (Figure 24) is constant throughout the double-layer region, except for local variations due to phase belts and slots. The magnetic field (Figure 25) is flat in the front half and rises to a different level almost twice as great in the second half. (As will be shown later, the higher level in the second half is not confirmed by the data.)

The sidebar voltage for Run 544 (Figure 26) is the most uniform of any of the runs, showing five equally spaced peaks.

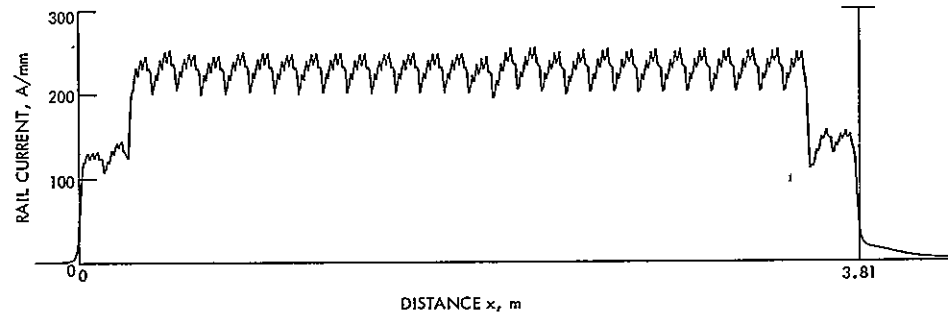

Figure 24. Theoretical amplitude of rail current at sensor C12 height in Run 544

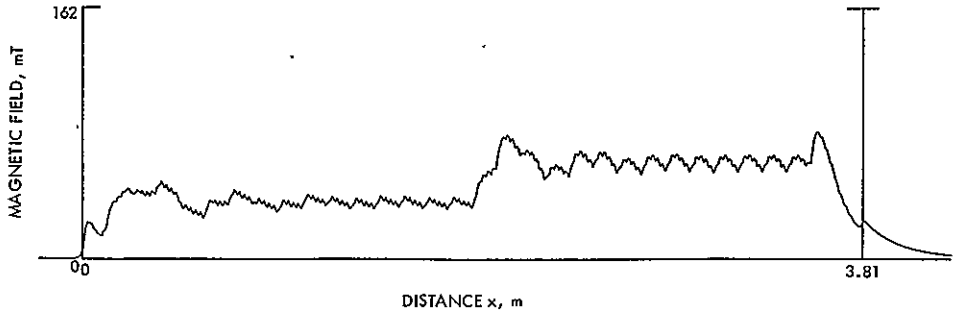

Figure 25. Theoretical amplitude of magnetic field at sensor F11 height in Run 544

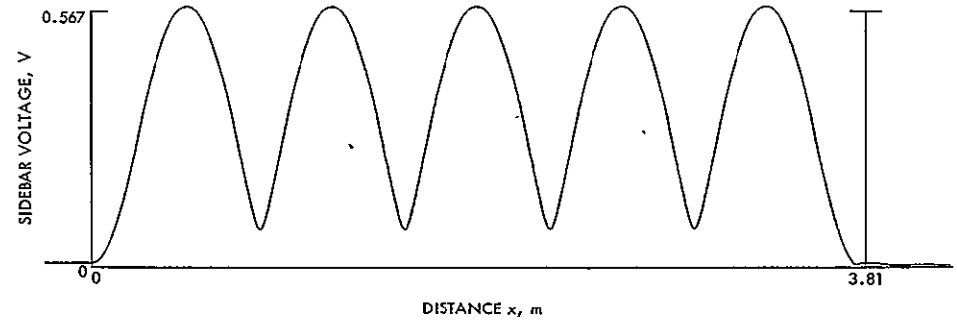

Figure 26. Theoretical amplitude of sidebar voltage in Run 544

V. CURRENT SENSOR FLUX

A. Method of Calculation

The flux λ linking the N turns of a current sensor due to a current filament I can be calculated from the geometry shown in Figure 27. If the current filamen is at longitudinal distance Δx from the center of the current sensor and at distance Δy from the plane of the sensor, then the magnetic field inside the sensor at distance x from the center is

$$B = \frac{\mu_0 I}{2\pi R} \tag{1}$$

where R is the slant distance from the current filament.

The flux through the cross-sectional area A of the sensor at the point x is the product of the area and the component of B in the x-direction.

$$\Phi = AB\frac{\Delta y}{R} \tag{2}$$

The total flux linking the turns of the sensor coil is the product of the number of turns and the average value of Φ over the length L of the sensor.

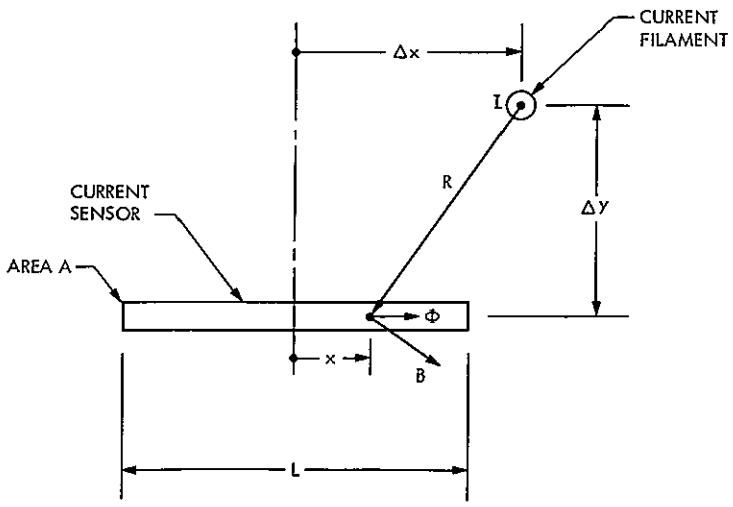

Figure 27. Geometry for calculation of flux through a current sensor

$$\lambda = \frac{N}{L} \int_{\frac{-L}{2}}^{\frac{L}{2}} \Phi \, dx \tag{3}$$

Substituting Φ from Equation (2) and noting that $R^2 = (\Delta x - x)^2 + \Delta y^2$, the total flux linking the N turns of the sensor is

$$\lambda = \frac{\mu_0 I AN}{2\pi L} \int_{\frac{-L}{2}}^{\frac{L}{2}} \frac{\Delta y}{(\Delta x - x)^2 + \Delta y^2} \, dx \tag{4}$$

Performing the integration, the sensor flux linkage is

$$\lambda = \frac{\mu_0 I AN}{2\pi L} \left[\tan^{-1} \left(\frac{\frac{L}{2} + \Delta x}{\Delta y} \right) + \tan^{-1} \left(\frac{\frac{L}{2} - \Delta x}{\Delta y} \right) \right] \tag{5}$$

This equation is the same as Equation (A-7) of Reference 2 for the case of negligible thickness of the sensor in the y-direction compared to the distance Δy from the current source.

The sensor constants derived from information in Reference 2 are: area A = 13.59 mm^2, length L = 34.9 mm, number of turns N = 1400 (for a series pair), and distance from plane of sensor to current sheet Δy = 2.797 mm.

The theoretical flux through a current-sensor pair is calculated by summing Equation (5) over all of the mesh currents in the motor (evaluated at the transverse position of the sensor). In practice, summing over as few as five meshes on each side of the sensor (2.5 slot pitches) gives the same value as summing over all the meshes; a summation over 100 meshes on each side is used here. The resulting value of sensor flux linkage λ is a complex number from which the amplitude and phase angle of the sensor flux can be determined.

B. Theoretical Sensor Flux Curves for the Experimental Runs

The theoretical current-sensor flux amplitudes as a function of distance x for the five test runs are plotted in Figures 28-32. By comparing these plots with the corresponding curves of rail current it can be seen that the sensor fluxes accurately follow the shape of the rail currents. The main difference is a smoothing of the smaller oscillations due to the averaging over the length of the sensor and over neighboring current filaments.

The scale coordinates for flux in Figures 28-32 are the values corresponding to one major unit of deflection on the oscillograph records as given in Reference 2, Table 3-2.

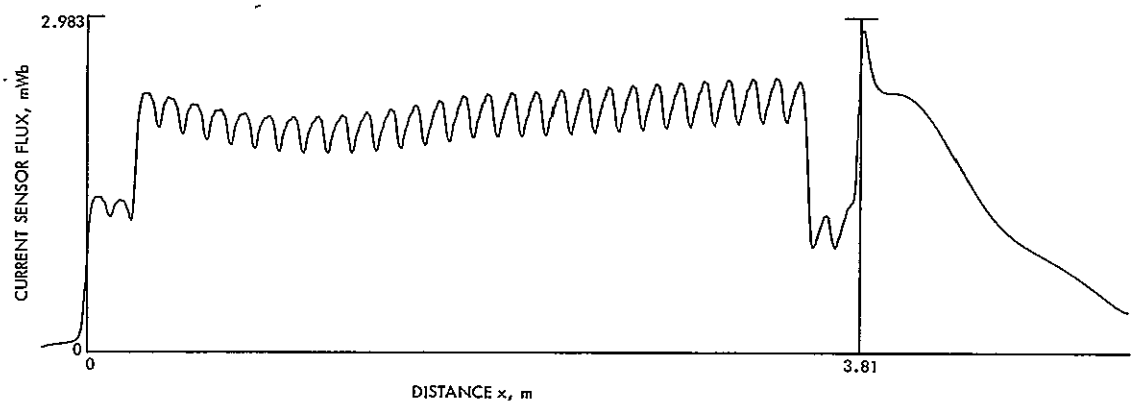

Figure 28. Theoretical amplitude of current sensor flux at sensor C12 height in Run 541

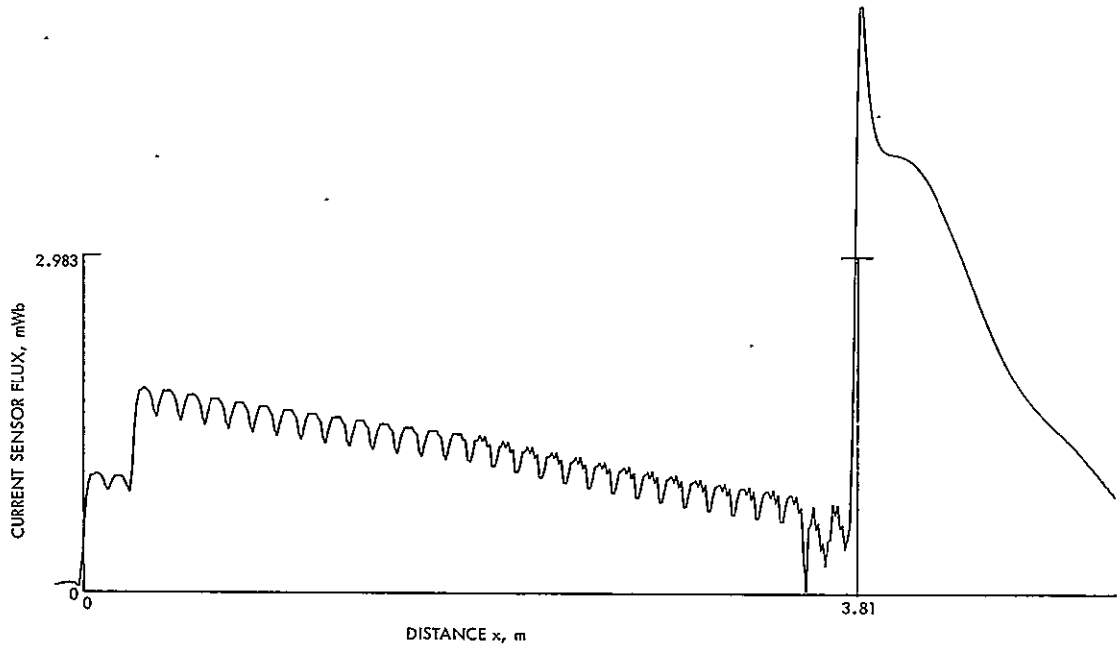

Figure 29. Theoretical amplitude of current sensor flux at sensor C12 height in Run 543

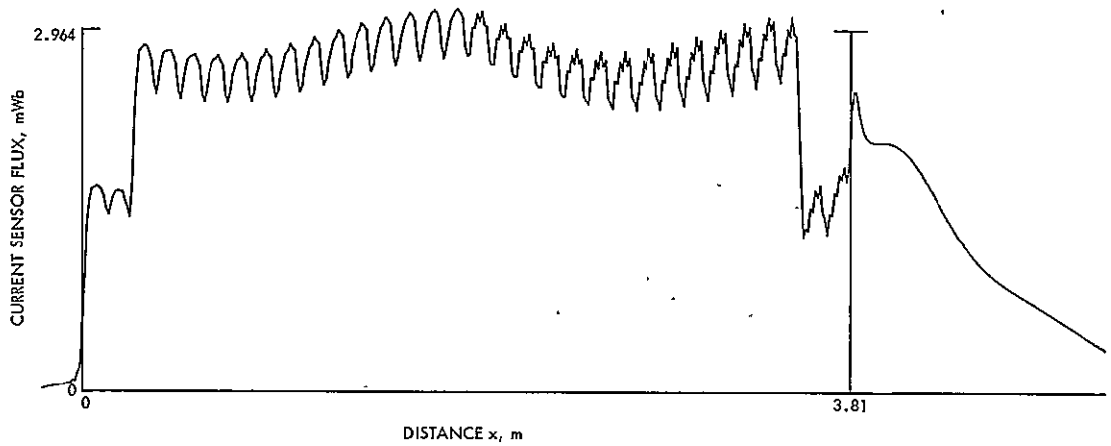

Figure 30. Theoretical amplitude of current sensor flux at sensor C12 height in Run 545

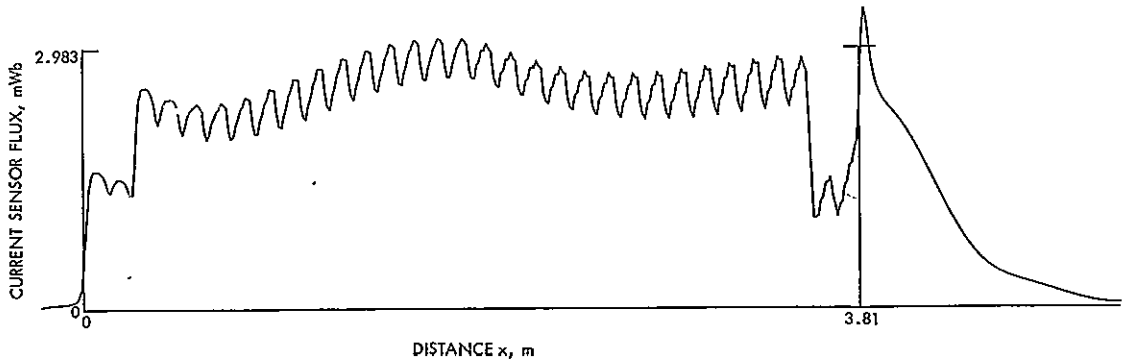

Figure 31. Theoretical amplitude of current sensor flux at sensor C13 height in Run 540

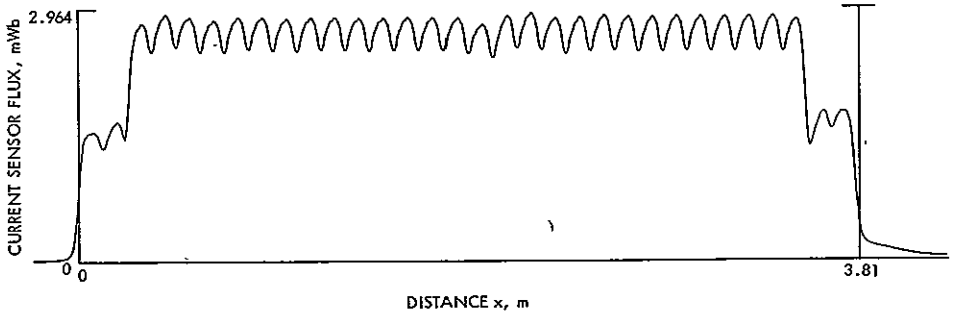

Figure 32. Theoretical amplitude of current sensor flux at sensor C12 height in Run 544

VI. CONSTRUCTION OF THEORETICAL OSCILLOGRAPH RECORDS

A. Calculation of Instantaneous Values

The theoretical longitudinal distributions of magnetic field, sidebar voltage, and current-sensor flux must be converted to theoretical distributions of the instantaneous values seen at the sensor stations as the vehicle passes. The method of conversion will be derived using the magnetic field as an example.

The calculated magnetic field B(k) at each mesh obtained from the mesh/matrix theory consists of a complex number such that the absolute value $|B(k)|$ is the rms value, and the angle

$$\theta_k = \tan^{-1} \frac{\text{Im } B(k)}{\text{Re } B(k)} \tag{6}$$

is the phase angle.

The phase angle is the angle of the field phasor at an arbitrary time $t = 0$. In the computations here, time is taken to be zero when the current in slot 1 (supplied by phase A) is zero and going positive. Thus, when phase A current has angle θ_A the time t is given by $\omega t = \theta_A$, where ω is the angular frequency.

If θ_A is the angle of phase A current when the entrance of the motor ($x = 0$) encounters the first sensor station, then $\omega t = \theta_A$ gives the time of encounter. Any other point x_k reaches the sensors after an additional time interval $\Delta t = x_k/U$, where U is the speed. Thus, the time t at which the sensors are at point x_k is given by

$$\omega t = \theta_A + \frac{\omega x_k}{U} \tag{7}$$

The angle of the field at mesh k at time t is

$$\underline{/B(k)_t} = \theta_k + \omega t$$

$$= \theta_k + \theta_A + \frac{\omega x_k}{U} \tag{8}$$

Thus, the instantaneous value of the field at any mesh k when the sensor station is opposite mesh k is

$$B(k)_t = \sqrt{2}\,|B(k)|\,\sin\left(\theta_k + \theta_A + \frac{\omega x_k}{U}\right) \qquad (9)$$

B. Oscillograph Record Construction

The method of constructing the theoretical oscillograph record of magnetic field at a given sensor in a given LIMRV run is as follows: The magnetic fields at each mesh are calculated from the mesh/matrix theory using the LIMRV constants and the operating conditions of the test run. The transverse distribution of the field is calculated from Bolton's theory using the same constants and the same operating conditions. The field in a slotted-rotor motor with the same constants and the same operating conditions is calculated from the equations in Reference 5, Section X. The mesh/matrix field values are then multiplied by the ratios of Bolton field at the sensor position to slotted-rotor field. (The ratio is a complex number, and the same correction is achieved by multiplying the amplitude by the ratios in Table 4, and shifting the phase by the angles in Table 4, for that sensor.) The result is the set of B(k) and θ_k values to be used in Equation (9).

The phase-A current angle at motor encounter with the sensor station, θ_A, is obtained, in principle, from the data (but see discussion on the next page). Substituting B(k), θ_k, θ_A, and the mesh coordinate x_k into Equation (9) gives the instantaneous field $B(k)_t$ at the particular sensor at the time it is at mesh k. The $B(k)_t$ values are then plotted as a function of the time at which each mesh reaches the sensor. This provides the theoretical oscillograph record.

The theoretical oscillograph records of current sensor flux and sidebar voltage are constructed in the same way.

In the mesh/matrix calculations used here, the mesh points extend from 0.2 m in front of the motor to 1.4 m behind. Three mesh points per slot pitch are used in the cases matching Run 541 and Run 544. Comparison calculations with two meshes per slot pitch for those cases show little change, and two meshes per slot pitch are used in the other cases. The total number of meshes is 459 with two meshes per slot pitch and 688 with three meshes per slot pitch.

C. Determination of Experimental Encounter Angle θ_A

The oscillograph records in Reference 2 include a trace identified as phase A current. This trace is found to be about 120 deg behind the position phase A current should occupy, based on the theoretical calculations, and therefore the recorded trace is assumed to be phase B. (The authors of Reference 2 agree that such a trace identification error could have occurred.)

The angle of the recorded phase current at encounter of the motor entrance with each sensor station, which is the angle θ_A (after the 120-deg correction), can be measured only crudely from the oscillograph records because the records consist of steps from digital sampling of the phase current. The uncertainty in θ_A is between 15 and 30 deg, depending on frequency, and the shapes of the theoretical oscillograph records change appreciably with that large a change in θ_A. Therefore, it is necessary to reverse the procedure and find the value of θ_A for the best match between the theoretical and experimental oscillograph records. When this is done, the best-fitting θ_A values agree with the experimental θ_A values within the uncertainty of the digital sampling time (0.5 ms) for all but one run, where the error is twice as great. The best-fitting θ_A values are compared with the experimental values in Table 5. The best-fitting θ_A values are the ones used for constructing the theoretical oscillograph records.

Table 5. Comparison between best-fit and experimental phase angles of phase A current at encounter

Run No.	Best-fit θ_A, deg	Experimental θ_A, deg
540	51	50 ± 13
541	-22	-40 ± 24
543	-169	-190 ± 21
544	-21	-75 ± 30
545	103	82 ± 30

D. Determination of Experimental Entrance and Exit Times

The position sensor on the vehicle did not provide a usable oscillograph recording, and it is necessary to determine the moment of arrival of the motor entrance at the sensor stations from the initial rise of the current sensor trace.

In addition, the oscillograph timing lines are about 4 percent in error; the timing-line interval noted on the oscillograph records in Reference 2 is 31.25 ms, but a count of the number of phase-current sampling steps between timing lines gives an interval closer to 30 m/s. Because of the time-base uncertainty, there is no way to identify the exit of the motor on the oscillograph records other than as the position of the final spike on the current-sensor traces.

As a result, when the theoretical oscillograph traces are plotted for superposition on the experimental traces, the entrance and exit positions must be set by matching the entrance rise and the exit spike of the theoretical current-sensor traces to the corresponding features on the experimental traces.

Because of the necessary matching of the entrance and exit features of the theoretical and experimental curves, and the required selection of θ_A for best fit, the agreement between the experimental and theoretical oscillograph curves is undoubtedly better than would have been the case if the data for entrance and exit position had been available and the data for encounter angle θ_A had been accurate enough to use.

VII. COMPARISON OF THEORETICAL AND EXPERIMENTAL OSCILLOGRAPH RECORDS

A. Comparisons for Run 541

Run 541 is selected for the most detailed comparison because it represents the highest-speed cruising condition. Also, the largest disagreement between the experimental and theoretical thrust and power occurs for this run: there is a 26 percent difference in thrust and a 21 percent difference in power (Table 3).

Figure 33 presents, as the black curve, the theoretical flux through sensor C12 in Run 541 as a function of time. The red curve is a copy of the experimental oscillograph record for the same sensor. (Note that the areas above and below the zero line are not equal. This does not imply net current, because the points on the curve correspond to different times.)

Figure 33 shows that the theoretical and experimental current-sensor fluxes, as seen by sensor C12 in Run 541, are almost identical up to the exit of the motor. Beyond the exit the curves differ by an amount that is equivalent to a 20-deg phase shift; at a time 20 deg (or 0.4 ms or 34 mm) earlier than the time in Figure 33 the theoretical and experimental curves have the best match beyond the exit.

The main difference between the theoretical and experimental curves inside the motor in Figure 33 is the difference in the position of the peaks due to the phase belts. It is possible that these differences are due only to experimental errors such as nonuniform vehicle speed or distortions in the oscillograph recording and reproduction.

Figure 34 compares the theoretical and experimental current sensor fluxes for sensor C11, the sensor located at the edge of the motor. In this case, there is considerable difference between the theoretical and experimental magnitudes. The theoretical sensor flux amplitude is about 25 percent less than the experimental flux, indicating that the rail current decreases less rapidly toward the edge of the motor than predicted by Bolton's theory and plotted in Figure 3.

Figure 35 compares the theoretical and experimental fluxes for current sensor C13 at the center of the motor ($z = 0$). At this position, the experimental flux is slightly less than the theoretical flux, again indicating a flatter current distribution than predicted by Bolton's theory.

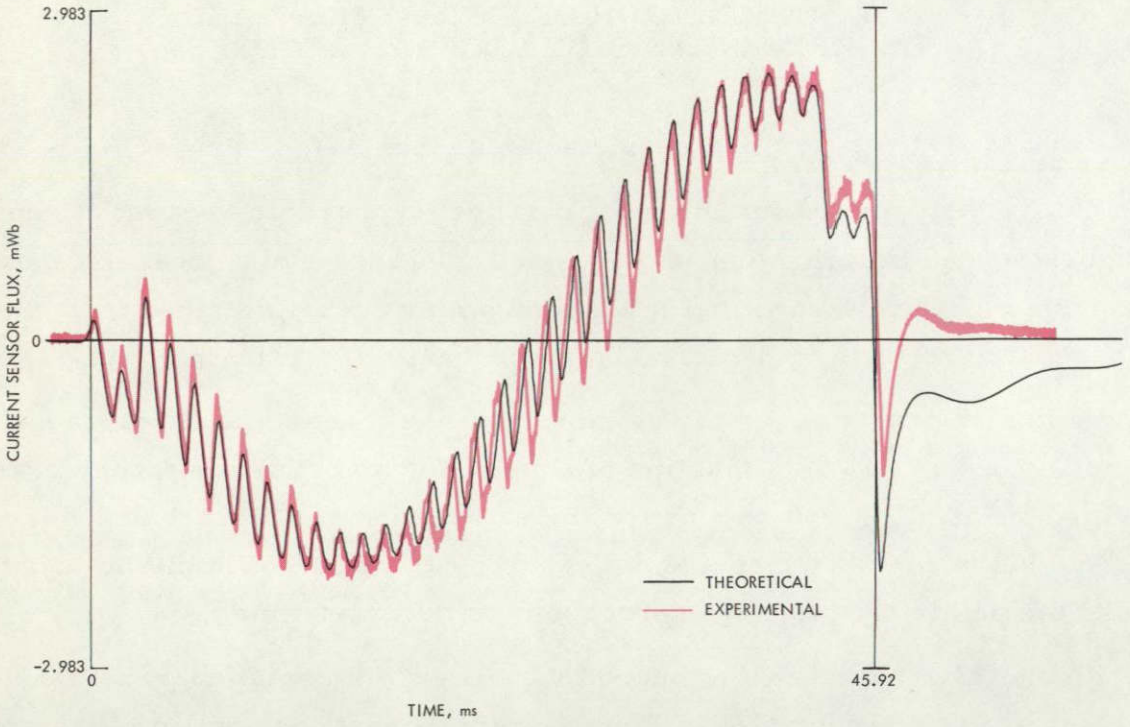

Figure 33. Comparison between theoretical and experimental fluxes through current sensor C12 in Run 541

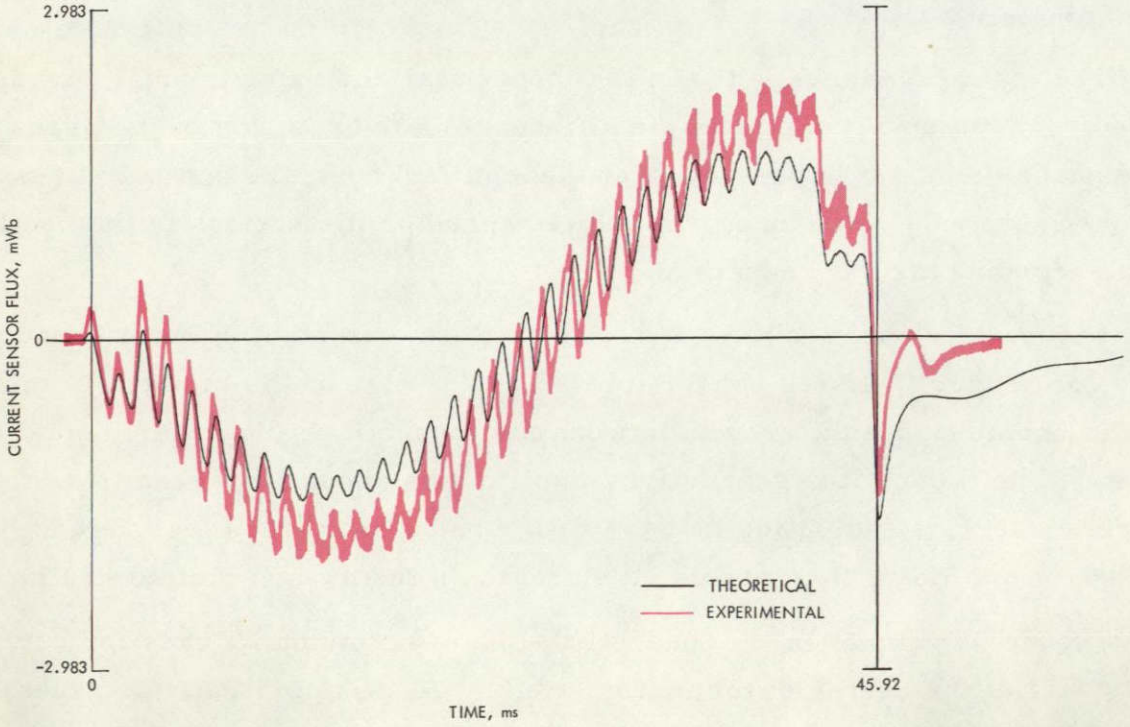

Figure 34. Comparison between theoretical and experimental fluxes through current sensor C11 in Run 541

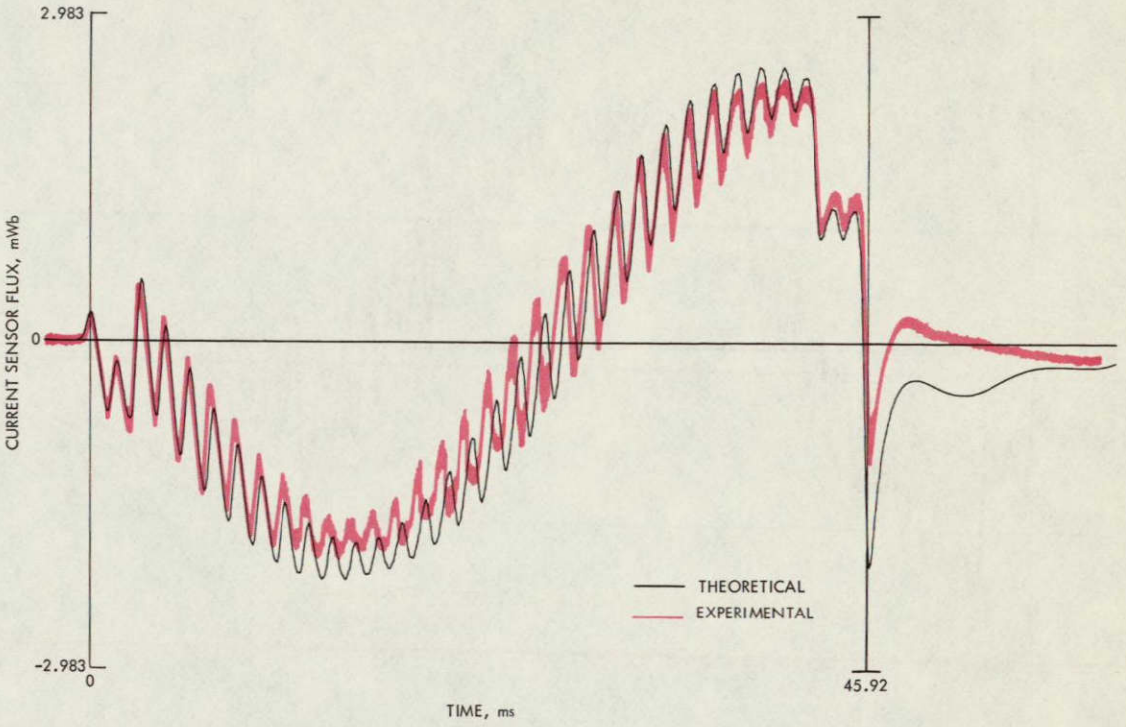

Figure 35. Comparison between theoretical and experimental fluxes through current sensor C13 in Run 541

In interpreting the differences between theoretical and experimental curves it should be kept in mind that the vertical axis (sensor output) values at a given point on the horizontal (time) axis depend on both amplitude and phase angle. It is not possible to determine whether a given deviation between theory and experiment at one such point is due to a difference between theoretical and experimental amplitudes or between theoretical and experimental phase angles. However, in cases where the oscillograph curves go through a half-cycle or more and reach a maximum or minimum, as in Figures 33, 34, and 35, the peaks can be identified as the amplitudes at those points, provided the longitudinal distribution is relatively flat. Thus, a comparison between theoretical and experimental peak magnitudes provides a rough comparison of amplitudes. An alternative method of comparing amplitudes, by reconstructing the phasor quantities from the data, is presented in Section VIII.

The theoretical and experimental current sensor fluxes at the second sensor station are compared in Figure 36. The sensor is C22 at the same z-position as sensor C12 in Figure 33. The theoretical and experimental curves

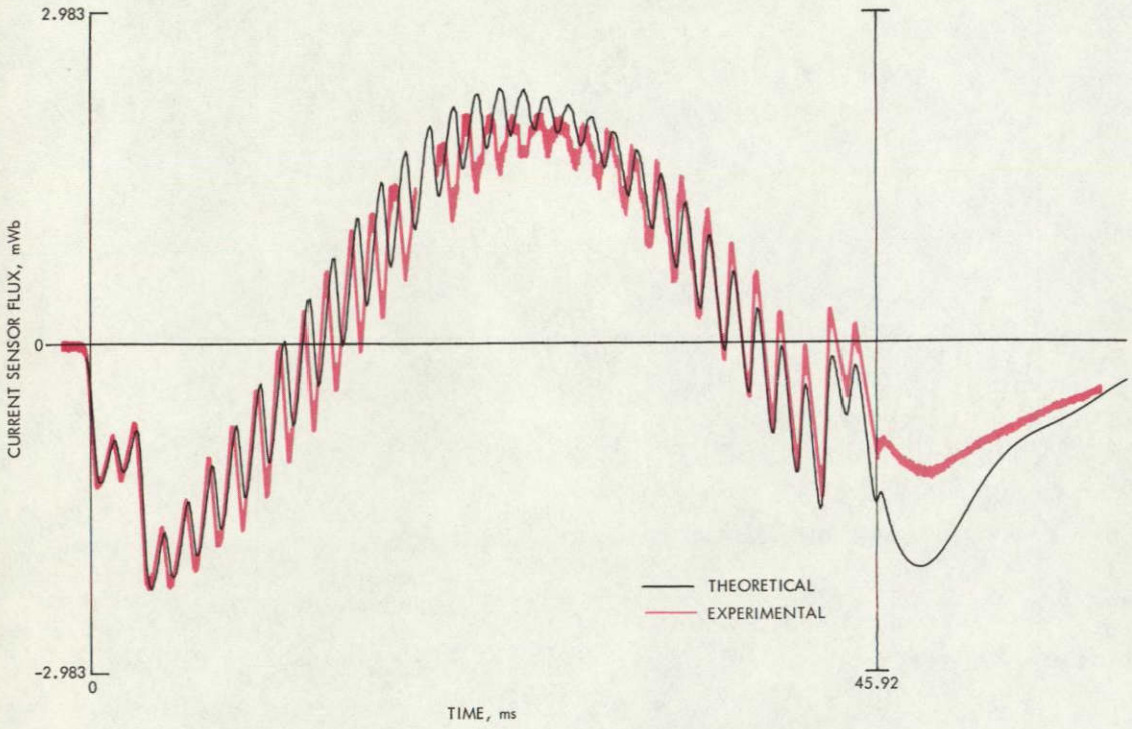

Figure 36. Comparison between theoretical and experimental fluxes through current sensor C22 in Run 541

agree within 10 percent inside the motor. The curves beyond the exit differ by an amount that can be explained by a 30-deg phase discrepancy. However, a smaller experimental than theoretical amplitude in this region is also consistent with the results.

Figure 37 compares the theoretical and experimental magnetic fields at sensor F12, located in the low-field region of the transverse distribution (Figure 3). The agreement is good in the first half of the motor, but the measured field is 25 percent less than theoretical at the exit of the motor.

Figure 38 compares the fields at sensor F11, located closer to the edge and at a field value 1.73 times that at sensor F12, according to Table 4. Figure 38 shows that, at the exit, the measured field at sensor F11 is about 1.5 times the measured field at sensor F12 (Figure 37), instead of the 1.73 factor of increase predicted.

The most significant results from Figure 38 are the higher experimental than theoretical field in the first peak, and the lower experimental than

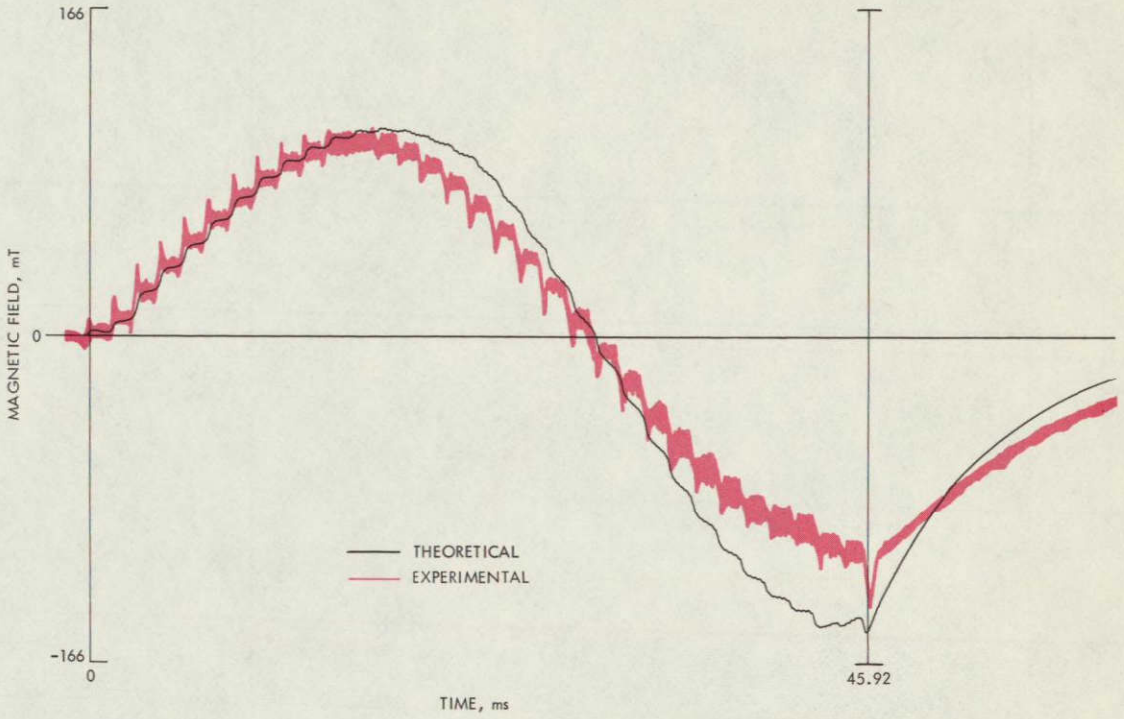

Figure 37. Comparison between theoretical and experimental magnetic fields at sensor F12 in Run 541

theoretical field in the second peak. This indicates that the field rises more rapidly in the first part of the motor than predicted by the mesh/matrix theory, but does not reach as high a final value as predicted.

The field comparisons at the second sensor station (Figure 39) indicate that the measured field is about 10 percent higher than theoretical at the center of the motor. Again, the field at the exit is below theory.

Figure 40 compares the theoretical and experimental sidebar voltages at the second sensor station (SB2). The agreement is poor. The theoretical voltages are half the measured values, and the positions of the peaks are a pole pitch in error. Furthermore, the theory predicts that the sidebar voltage remains high for at least a motor length in front and behind the motor. The measurements show this to be incorrect; the sidebar voltage is zero until the motor reaches the sidebar voltage contacts. After the motor passes, the experimental voltage persists, but this may be due only to the fringing field from the sides of the motor acting on the sidebar voltage leads, since opposite behavior is seen for

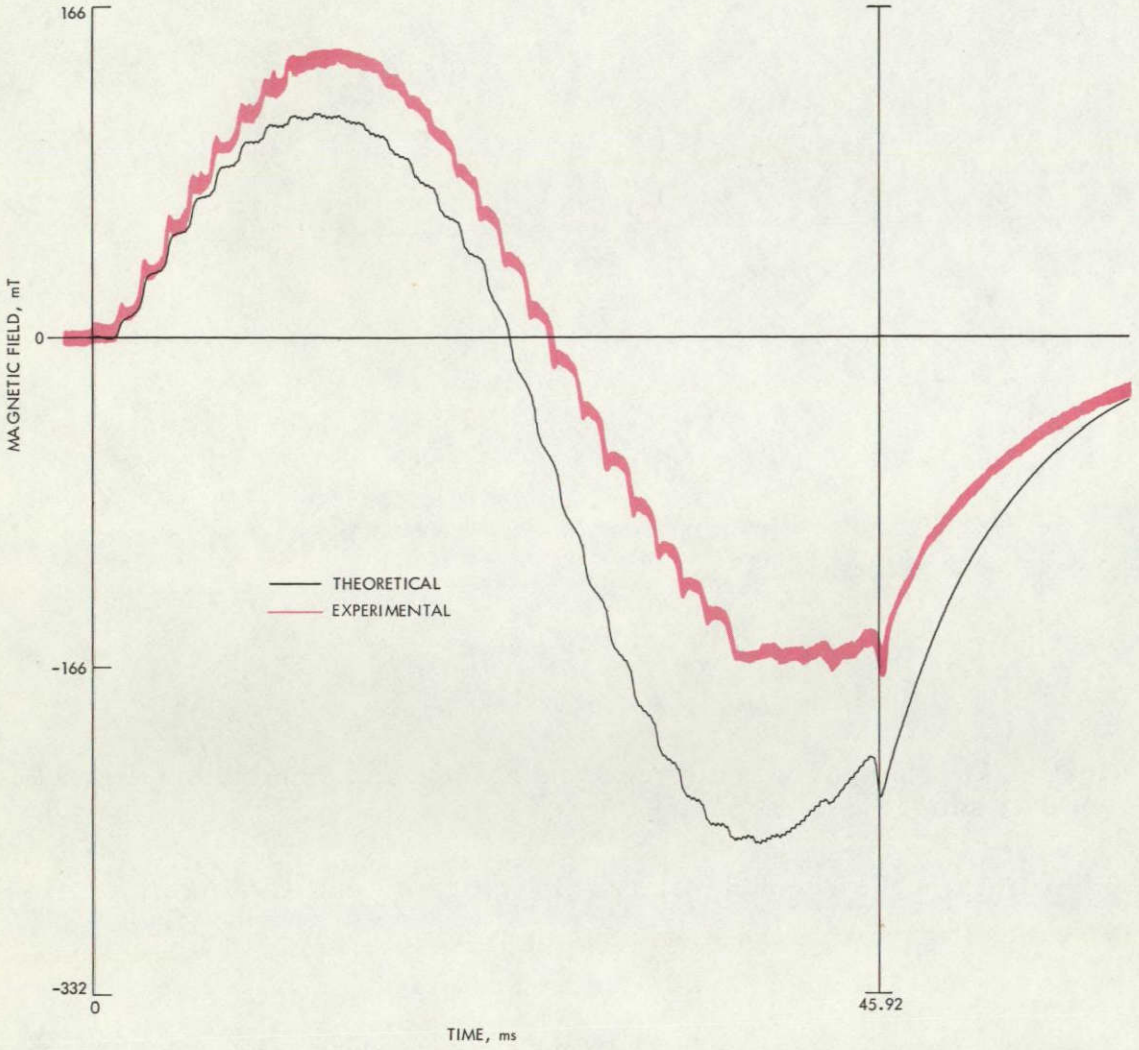

Figure 38. Comparison between theoretical and experimental magnetic fields at sensor F11 in Run 541

the SB1 voltage in the oscillograph records of Reference 2. The SB1 leads run toward the direction of the oncoming vehicle, and the fringing field pickup occurs prior to motor arrival.

Do the current and field comparisons shed any light on the large discrepancy between the theoretical and experimental thrusts for Run 541? The theoretical thrust is 26 percent less than the experimental thrust. Either the theoretical current or the theoretical field, or both, should be below the experimental values.

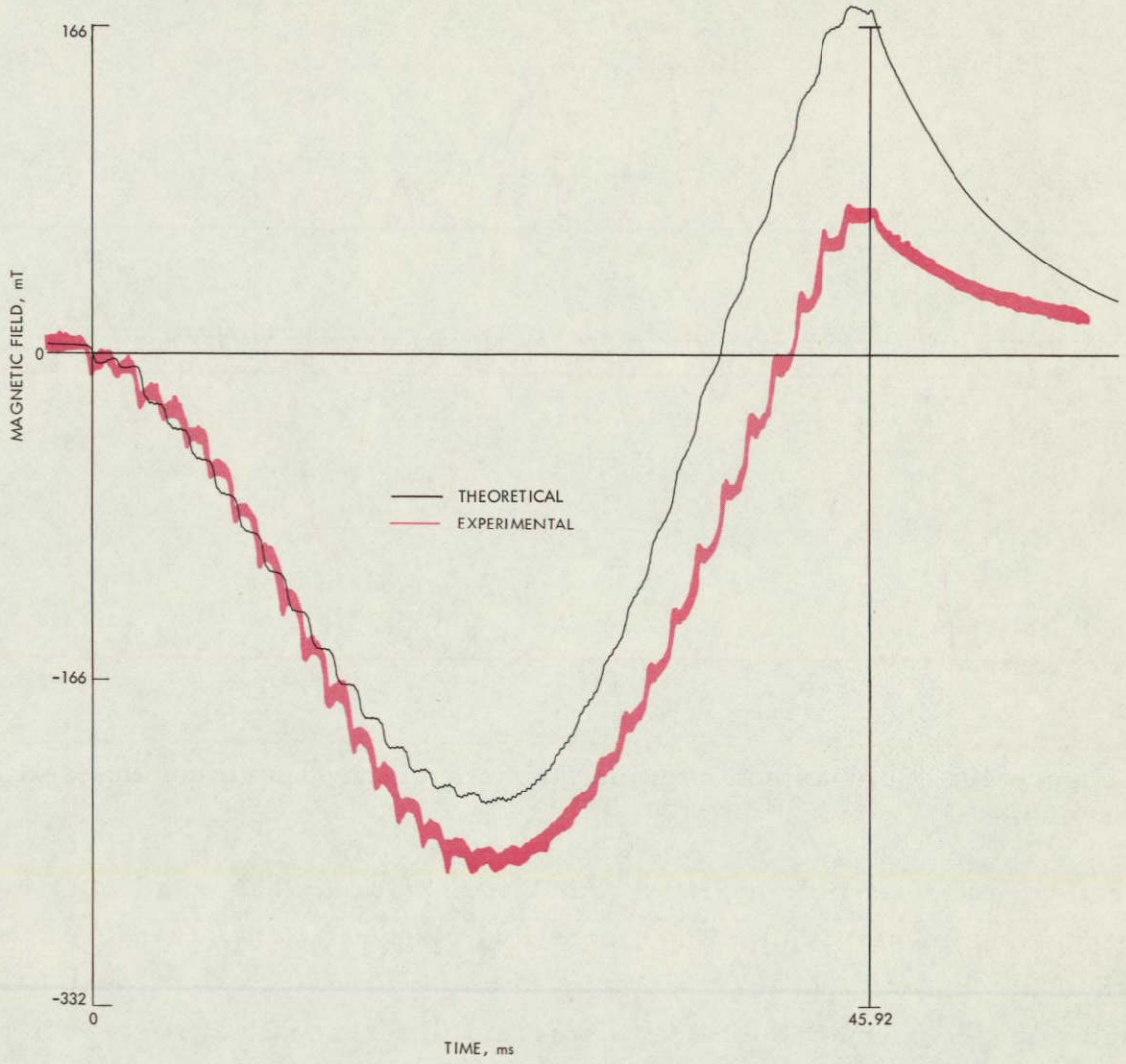

Figure 39. Comparison between theoretical and experimental magnetic fields at sensor F21 in Run 541

The theoretical current is equal to or slightly greater than the experimental current, both on the centerline of the motor (Figure 35) and halfway to the edge (Figures 33 and 36). However, the theoretical current is about 25 percent less than the experimental current at the edge of the motor (Figure 34).

The theoretical magnetic field is about 30 percent less than the experimental magnetic field in the first half of the motor, at a height three fourths of the way between the centerline and the edge (Figure 38), but is as much as twice the experimental field in the second half of the motor (Figures 38 and 39). The

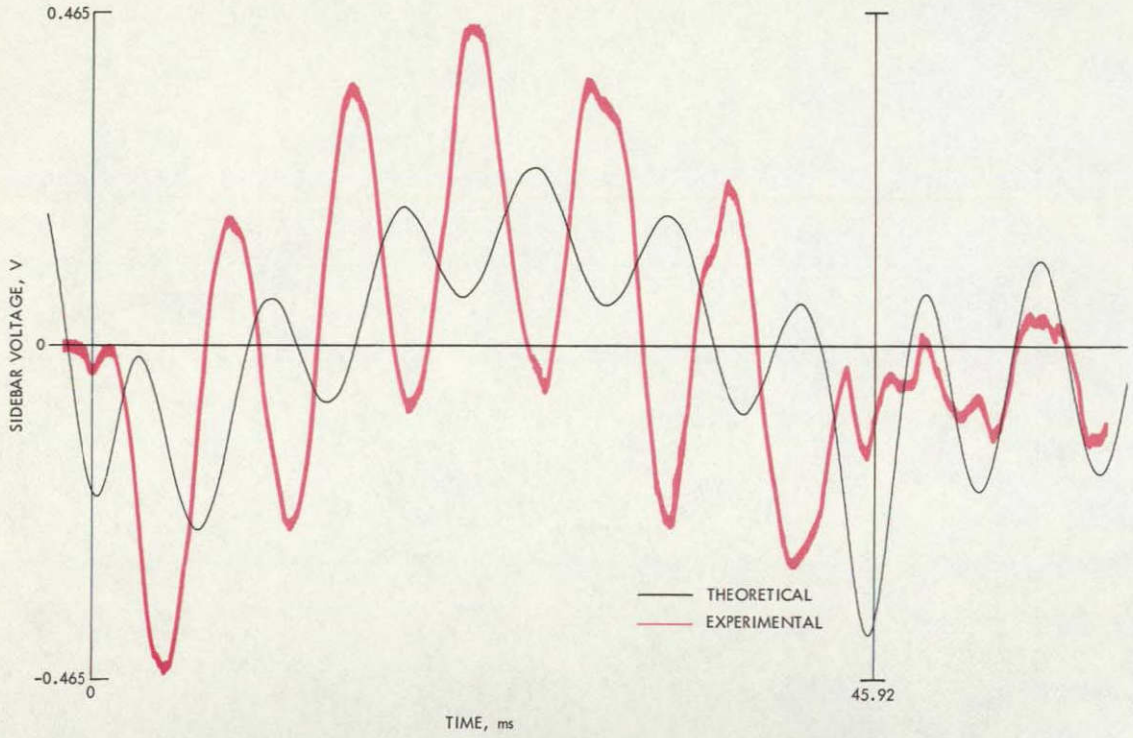

Figure 40. Comparison between theoretical and experimental sidebar voltages at contact SB2 in Run 541

theoretical magnetic field near the centerline (Figure 37) is equal to or higher than the experimental field. The theoretical magnetic field, averaged over the length of the motor, appears to be at least as large as the experimental field and probably larger. Thus, the field and current differences do not seem to provide sufficient explanation for the 26 percent lower theoretical than experimental thrust.

A possible explanation for the low theoretical thrust is the neglect of fringing field outside the edges of the motor in the theory. Such an explanation is advanced by Bolton in Reference 3 to account for theoretical thrust values about 8 percent lower than experimental in his own static tests of a linear motor. Bolton is able to bring the theoretical and experimental thrusts into agreement by adding one airgap length to the motor width ($c \rightarrow c + g$) to account for the fringing field. In the LIMRV motor this procedure would increase the theoretical thrust by 15 percent and increase the ratio of theoretical to experimental thrusts for Runs 540, 541, 544, and 545 to 0.94, 0.85, 0.92, and 0.93, respectively. A possible further effect might be that the thrust contribution of the fringing field does not decrease as rapidly with speed as the thrust inside the

motor, thus causing the relative contribution of the fringing-field thrust to increase with speed. And, of course, there is the possibility that the thrust data are in error.

B. Comparisons for Run 543

The oscillograph records for Run 543, the nearly zero-slip run, are of particular interest because the traces show the amplitudes directly (with a factor of proportionality depending on phase angle at encounter).

Figure 41 shows the theoretical and experimental fluxes through current sensor C12. At the time of arrival at this sensor station, the fundamental component of the rail current is close to zero, and only the oscillations due to the phase belts remain. The theoretical and experimental curves agree closely.

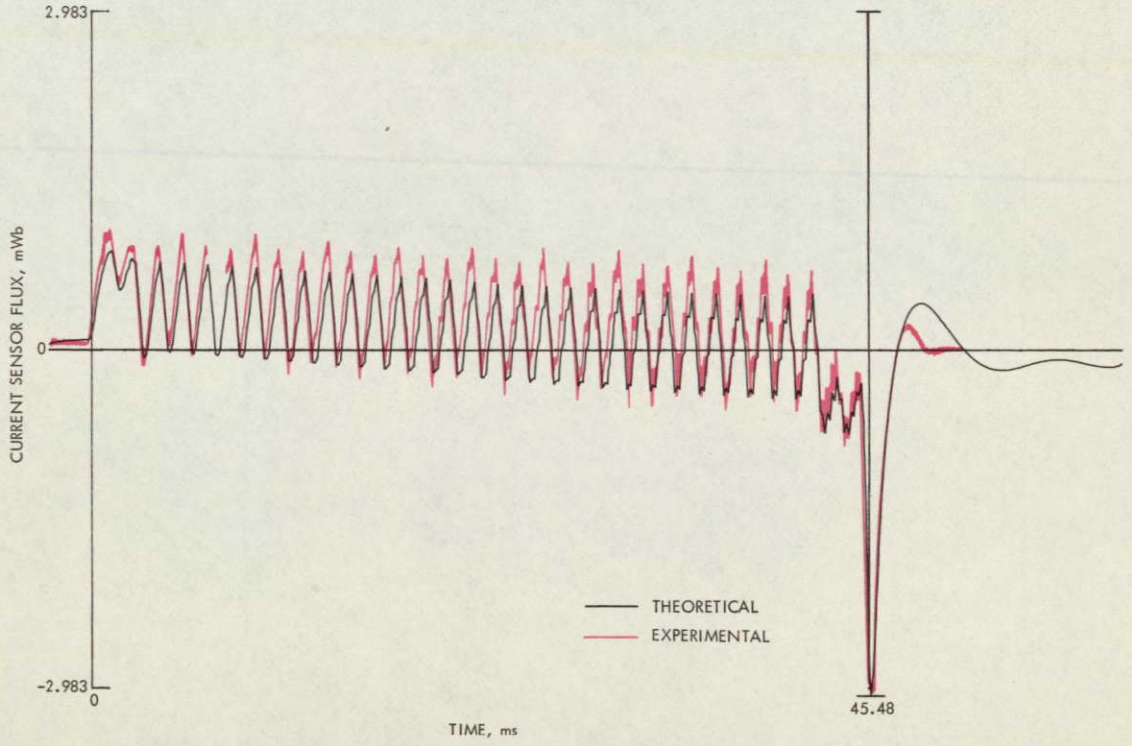

Figure 41. Comparison between theoretical and experimental fluxes through current sensor C12 in Run 543

At the time of arrival at the second sensor station (Figure 42) the rail current is close to maximum, and the current-sensor trace is essentially an amplitude trace. The theoretical curve in Figure 42 has the same shape as the amplitude curve in Figure 29, except for the reversal of the current beyond the exit in Figure 42 because of a 180-deg phase shift at the exit. The measured current in the second half of the motor is 50 percent higher than theoretical, and the measured peak at the exit is less than theoretical.

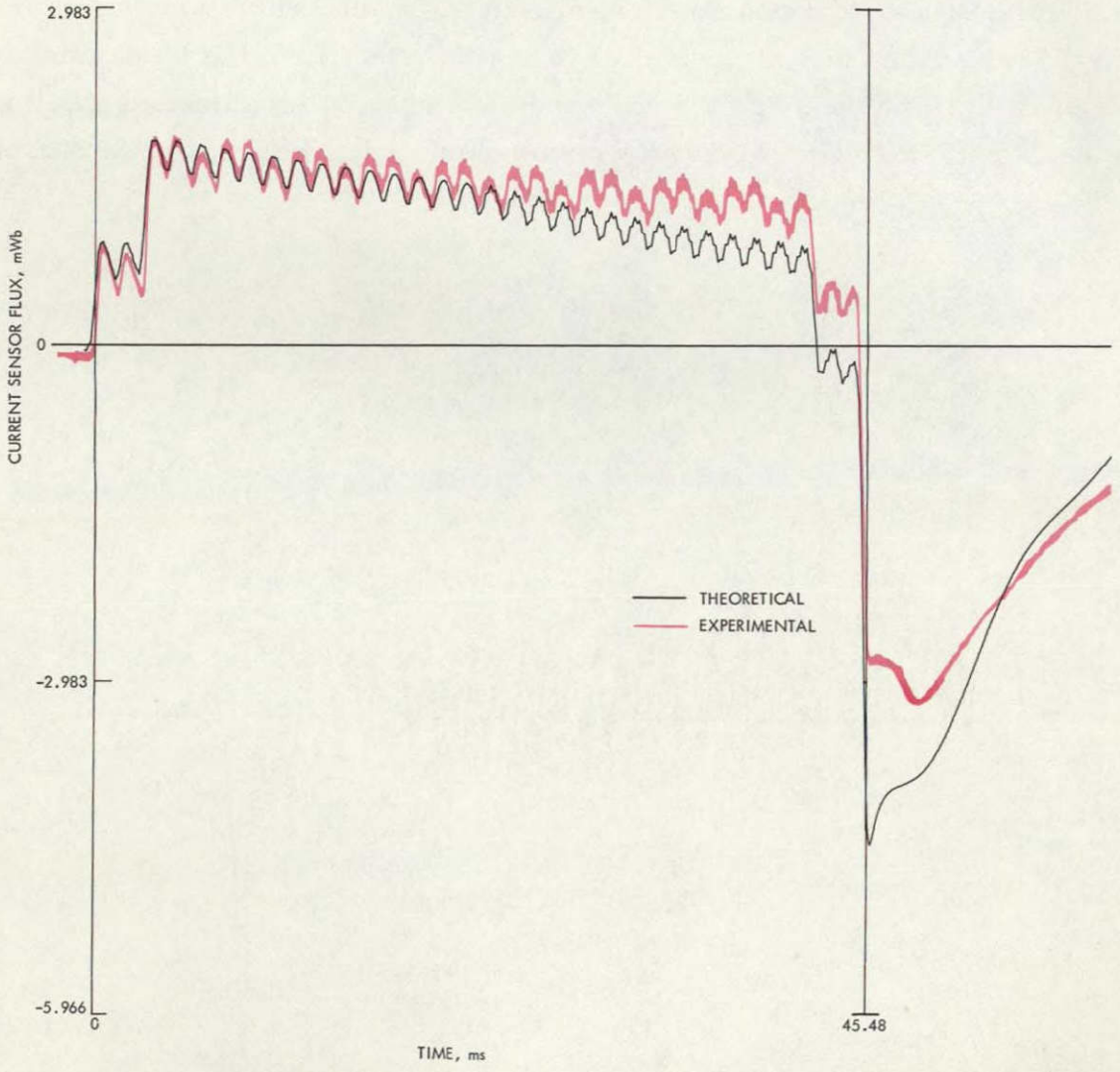

Figure 42. Comparison between theoretical and experimental fluxes through current sensor C22 in Run 543

The theoretical and experimental magnetic fields at sensor F11 are compared in Figure 43. The recording system evidently suffered a malfunction near the time of peak field, but up to that time the measured field amplitude is about 50 percent larger than the theoretical field. In the decay region the theoretical and experimental curves agree closely.

The magnetic field has just passed through zero at the time of arrival at the second sensor station (Figure 44), and the experimental field is twice the theoretical field. A phase shift of only 10 deg, however, would account for the difference.

As shown in Figure 45, the measured sidebar voltage is about 20 percent less than the theoretical sidebar voltage, and the peaks are shifted half a pole pitch.

C. Comparisons for Run 545

The theoretical and experimental current sensor fluxes at sensors C12 and C23 in Run 545 (the high-speed, medium-slip run) are compared in Figures 46 and 47, respectively. The agreement is good in both cases.

The theoretical and experimental magnetic fields at sensors F11 and F12 are compared in Figures 48 and 49, respectively. The agreement is poor. At sensor F11 the measured field in the second half of the motor is only half of the theoretical field. At sensor F12 the measured field in the first half of the motor is twice the theoretical field. The fields will be compared again in Section VIII using amplitude reconstruction.

The experimental sidebar voltage trace in Run 545 was not clear enough for comparison.

D. Comparisons for Run 540

Figures 50 and 51 present the current sensor fluxes at sensors C13 and C23, respectively, in Run 540 (the medium-speed, low-slip run). The theoretical and experimental curves agree closely. Figures 52 and 53 present the magnetic fields at sensors F11 and F21, respectively. The theoretical and experimental magnetic fields agree within 30 percent. The fields will be compared again in Section VIII.

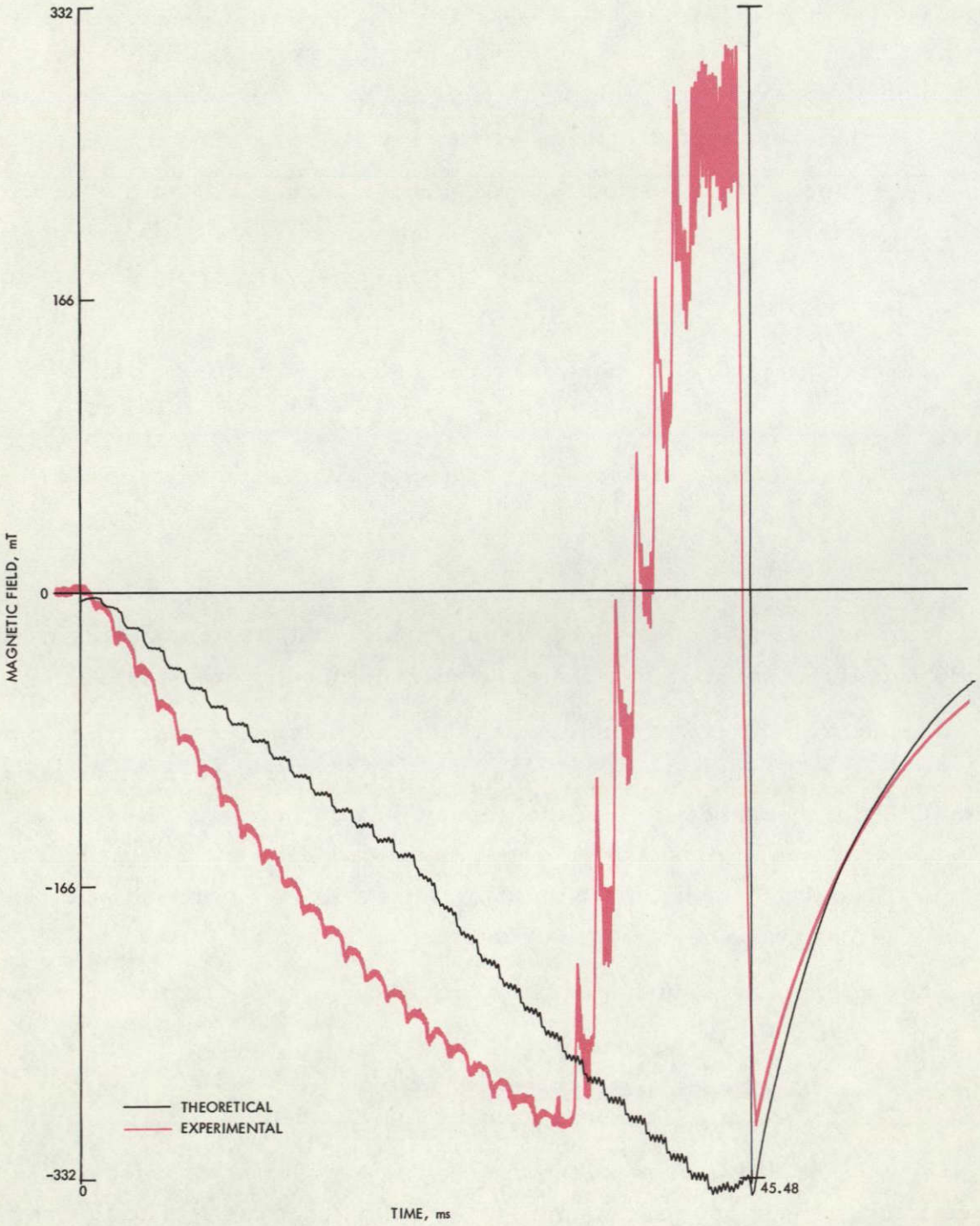

Figure 43. Comparison between theoretical and experimental magnetic fields at sensor F11 in Run 543

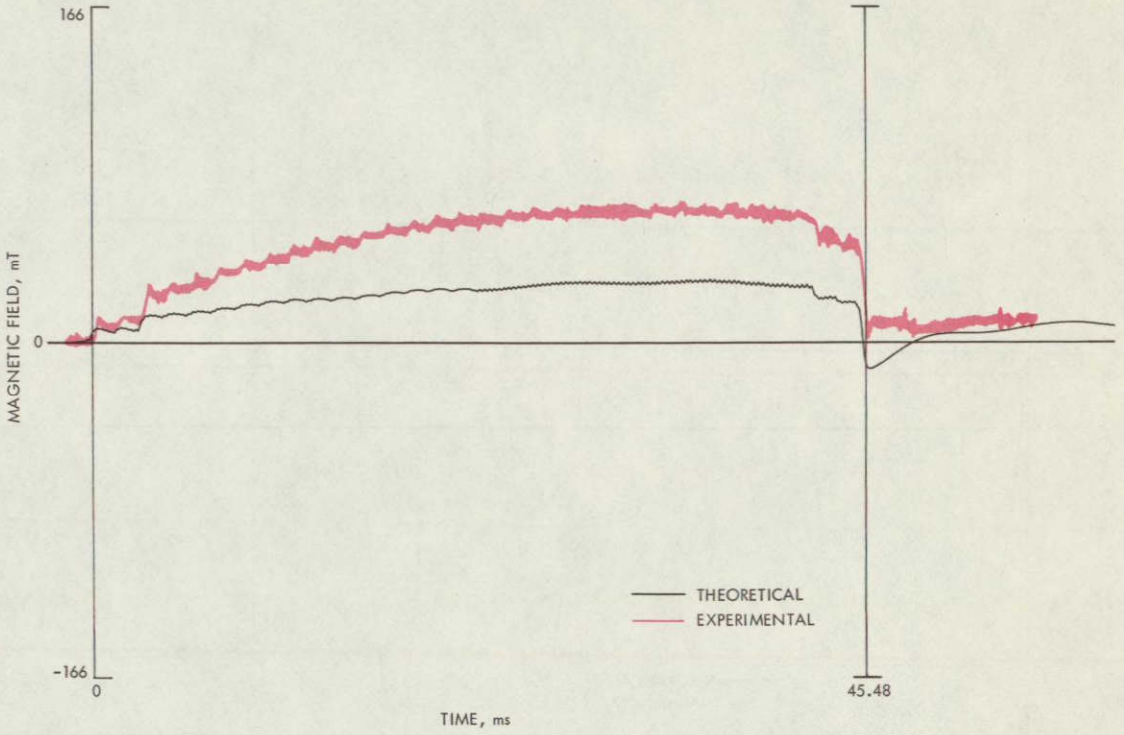

Figure 44. Comparison between theoretical and experimental magnetic fields at sensor F21 in Run 543

The measured sidebar voltage (Figure 54) has about twice the amplitude of the theoretical sidebar voltage.

E. Comparisons for Run 544

At the high slip of Run 544 the currents and fields seen by the sensors go through many cycles during passage of the motor. Figure 55 shows the flux through current sensor C22. The theoretical and experimental curves agree closely.

Figure 56 shows the magnetic field at sensor F11. The theoretical and experimental curves agree closely up to the middle of the motor, but then the theoretical amplitude almost doubles (as previously seen in Figure 25), whereas the measured field shows no increase.

The theoretical and experimental sidebar voltages for Run 544 are compared in Figure 57. The agreement is the best of any of the runs; the shapes of the curves agree closely, although the measured amplitude is about 20 percent greater than the theoretical amplitude.

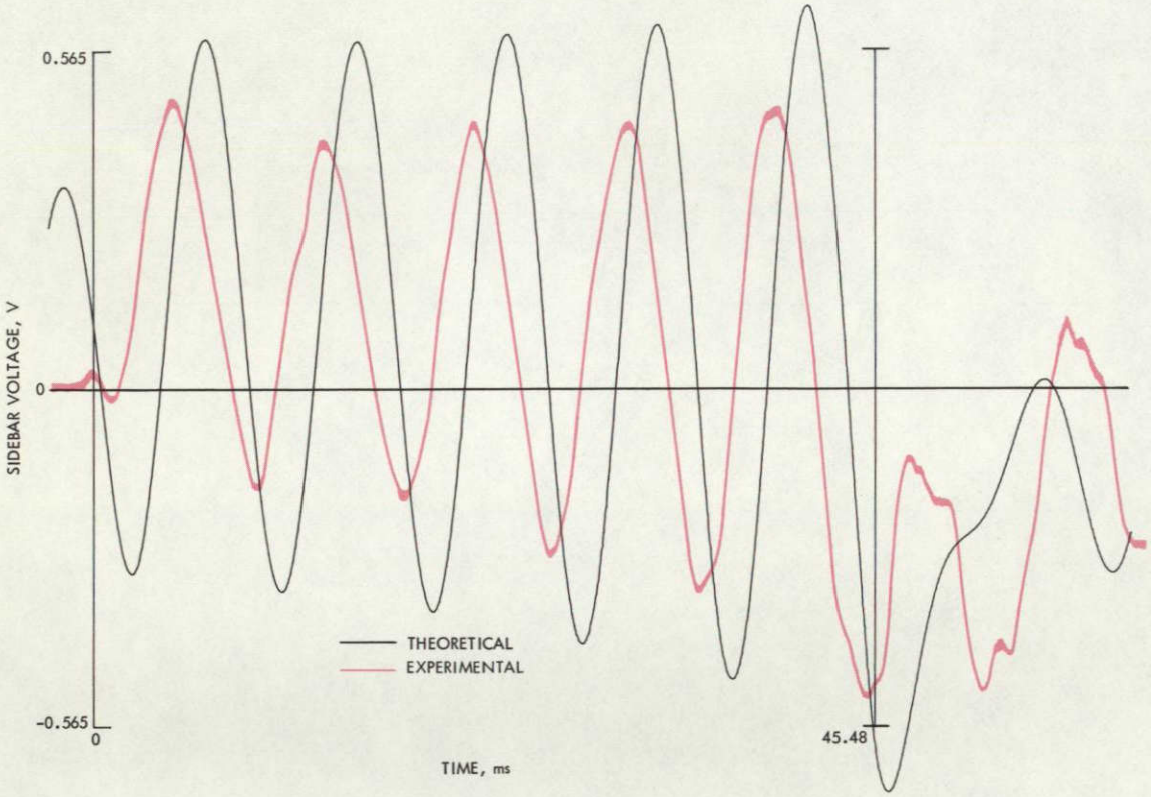

Figure 45. Comparison between theoretical and experimental sidebar voltages at contact SB2 in Run 543

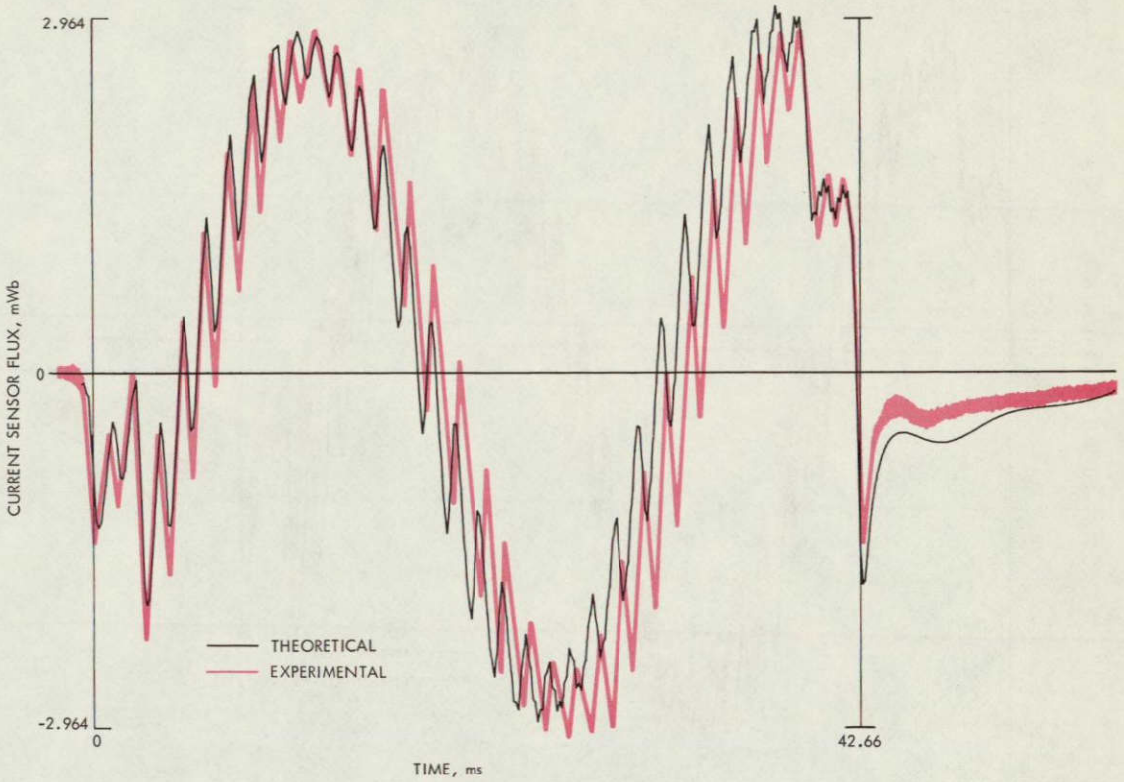

Figure 46. Comparison between theoretical and experimental fluxes through current sensor C12 in Run 545

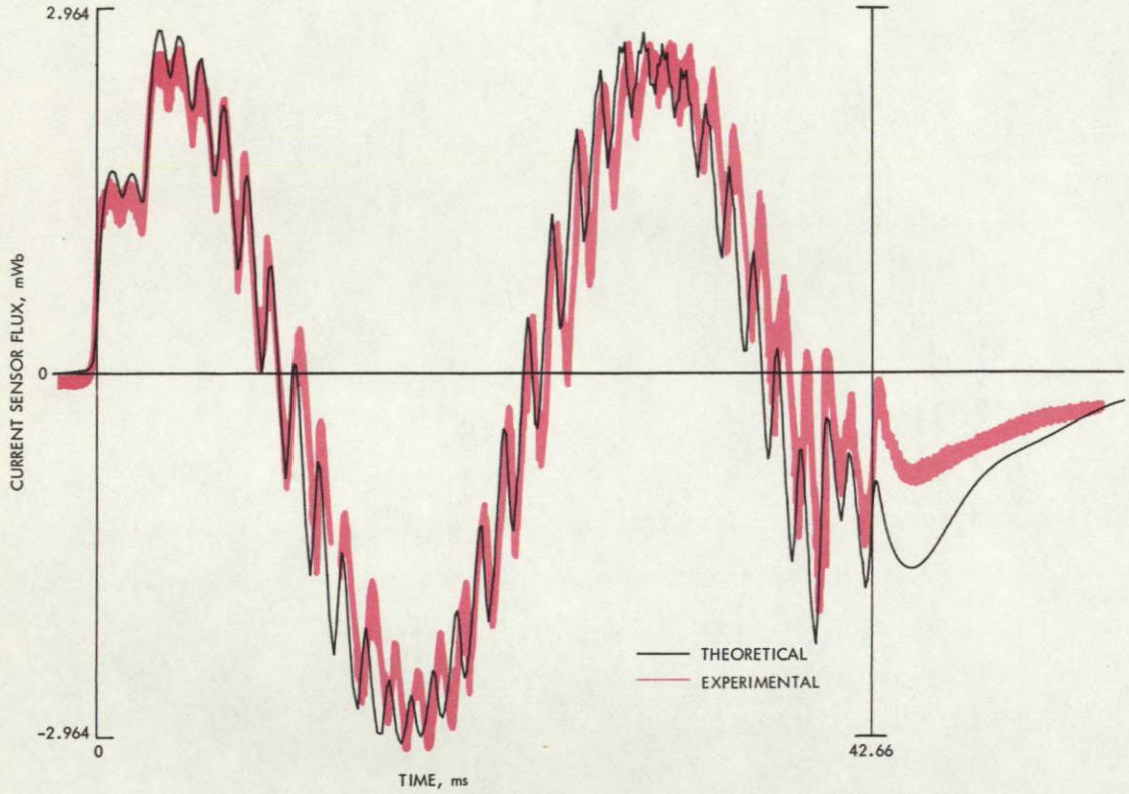

Figure 47. Comparison between theoretical and experimental fluxes through current sensor C23 in Run 545

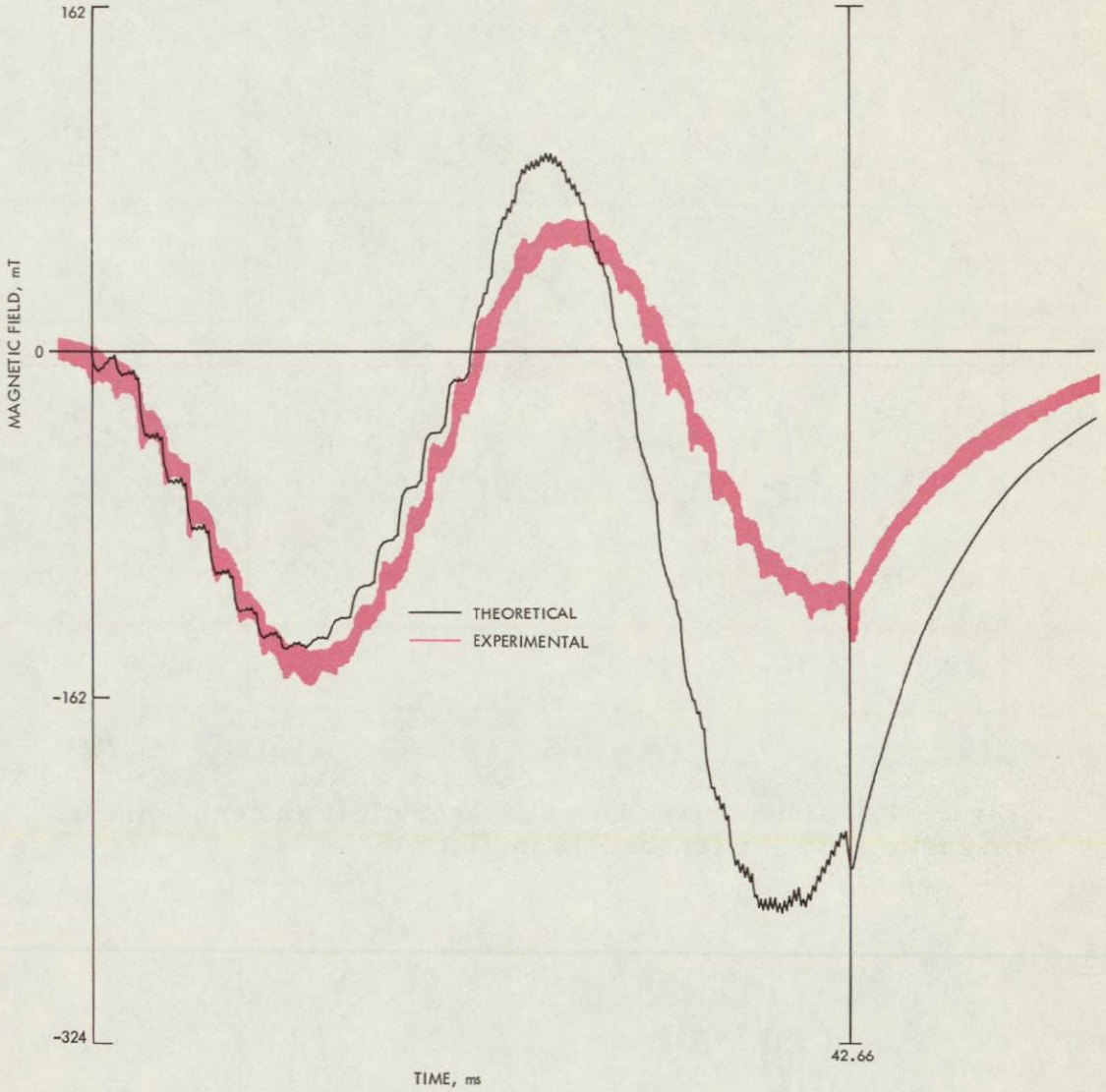

Figure 48. Comparison between theoretical and experimental magnetic fields at sensor F11 in Run 545

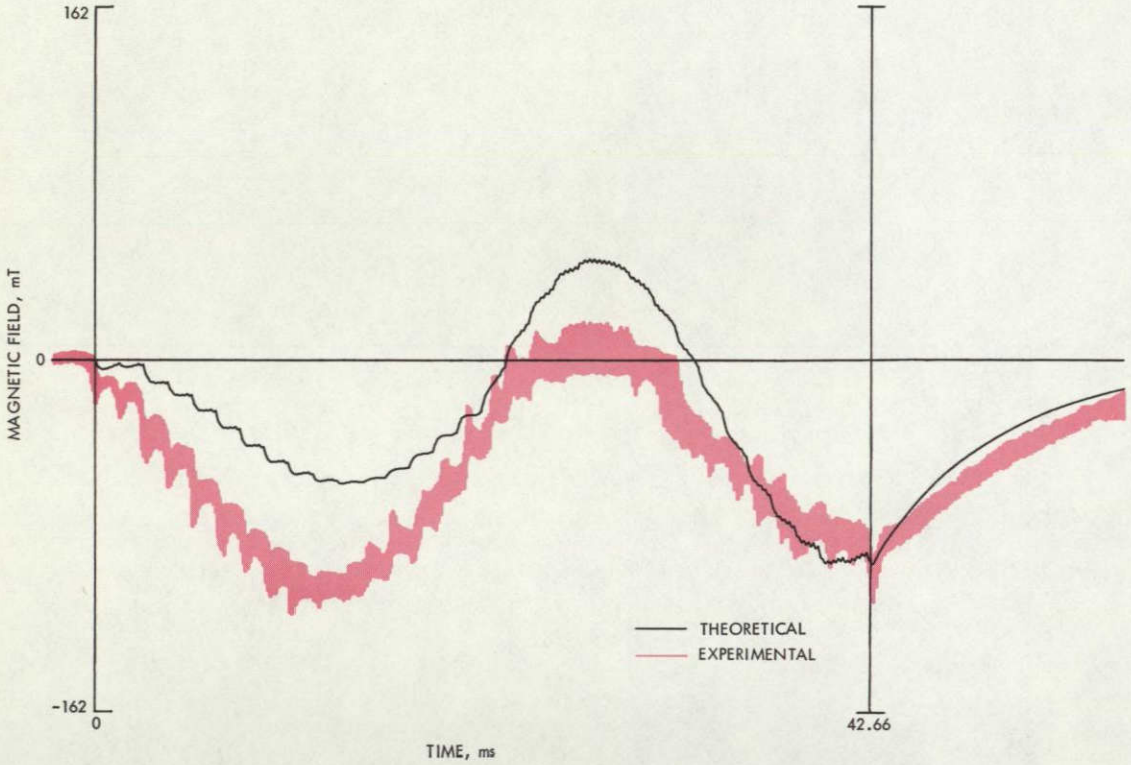

Figure 49. Comparison between theoretical and experimental magnetic fields at sensor F12 in Run 545

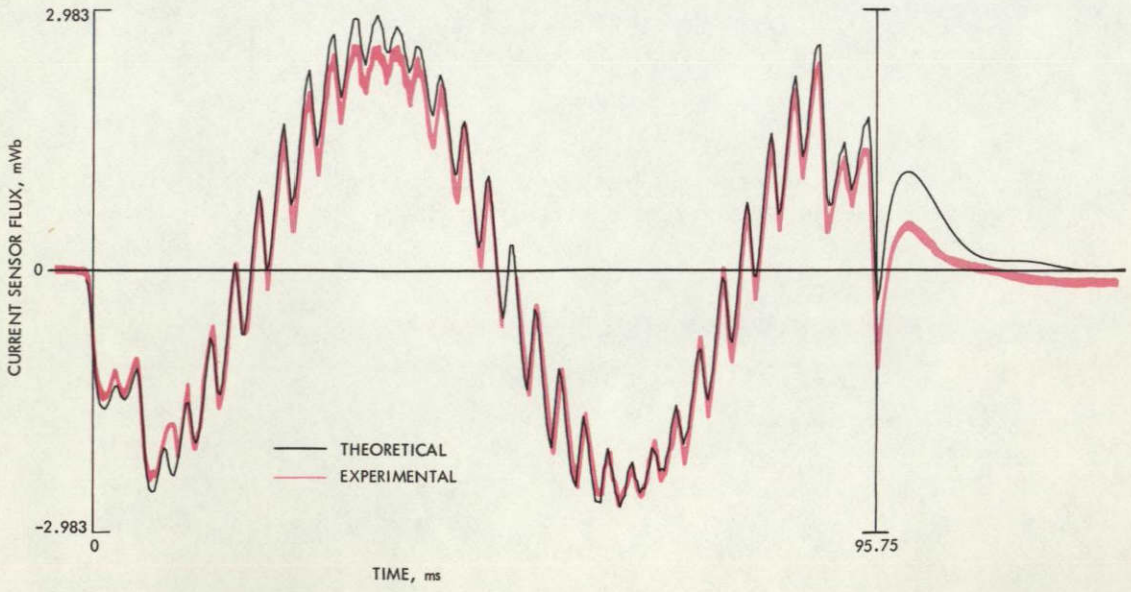

Figure 50. Comparison between theoretical and experimental fluxes through current sensor C13 in Run 540

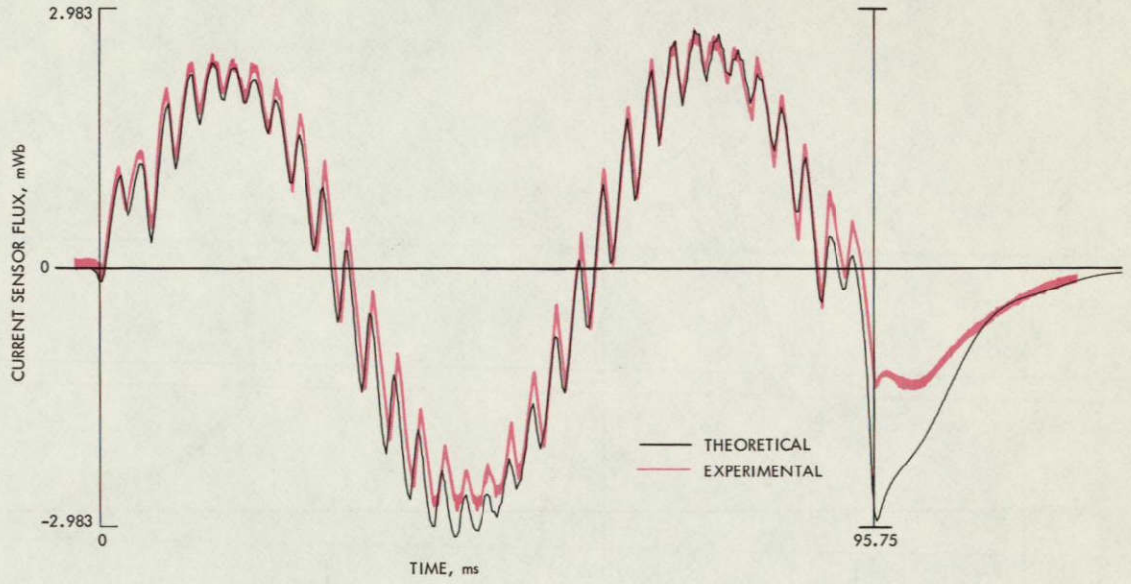

Figure 51. Comparison between theoretical and experimental fluxes through current sensor C23 in Run 540

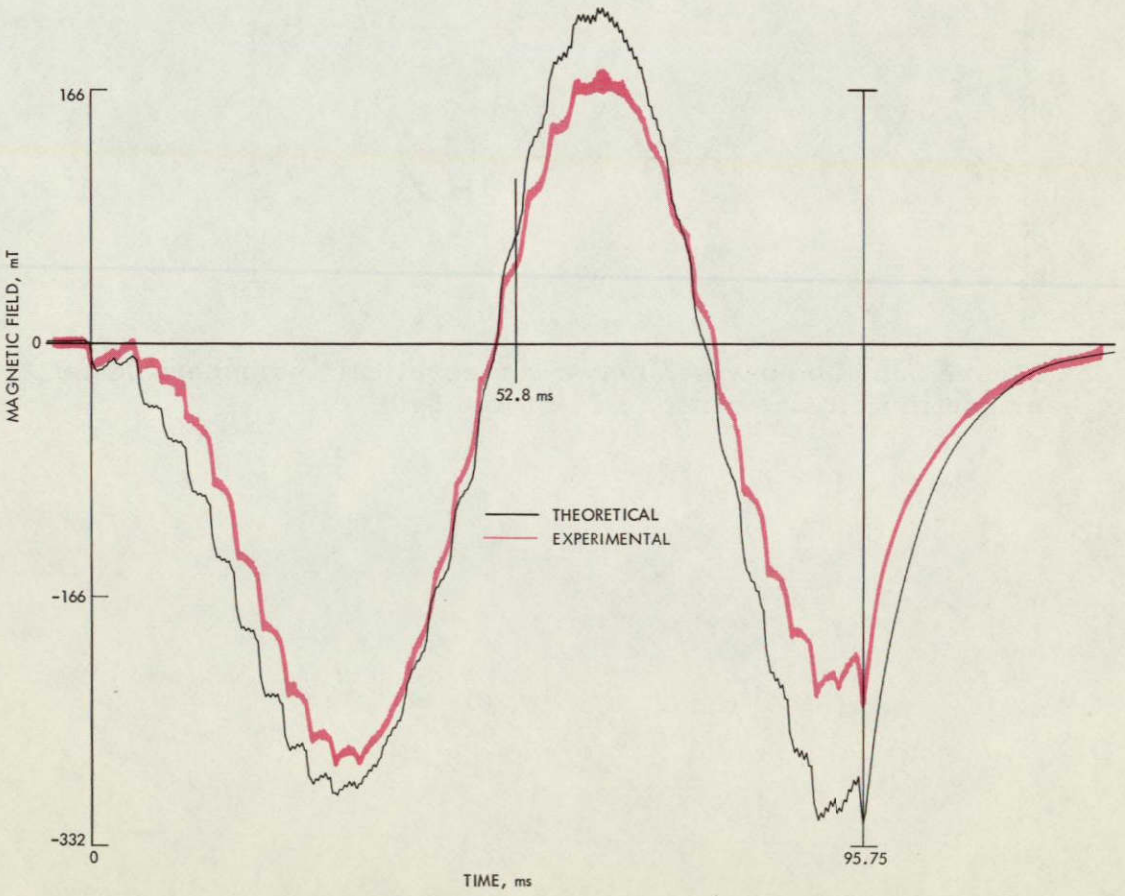

Figure 52. Comparison between theoretical and experimental magnetic fields at sensor F11 in Run 540

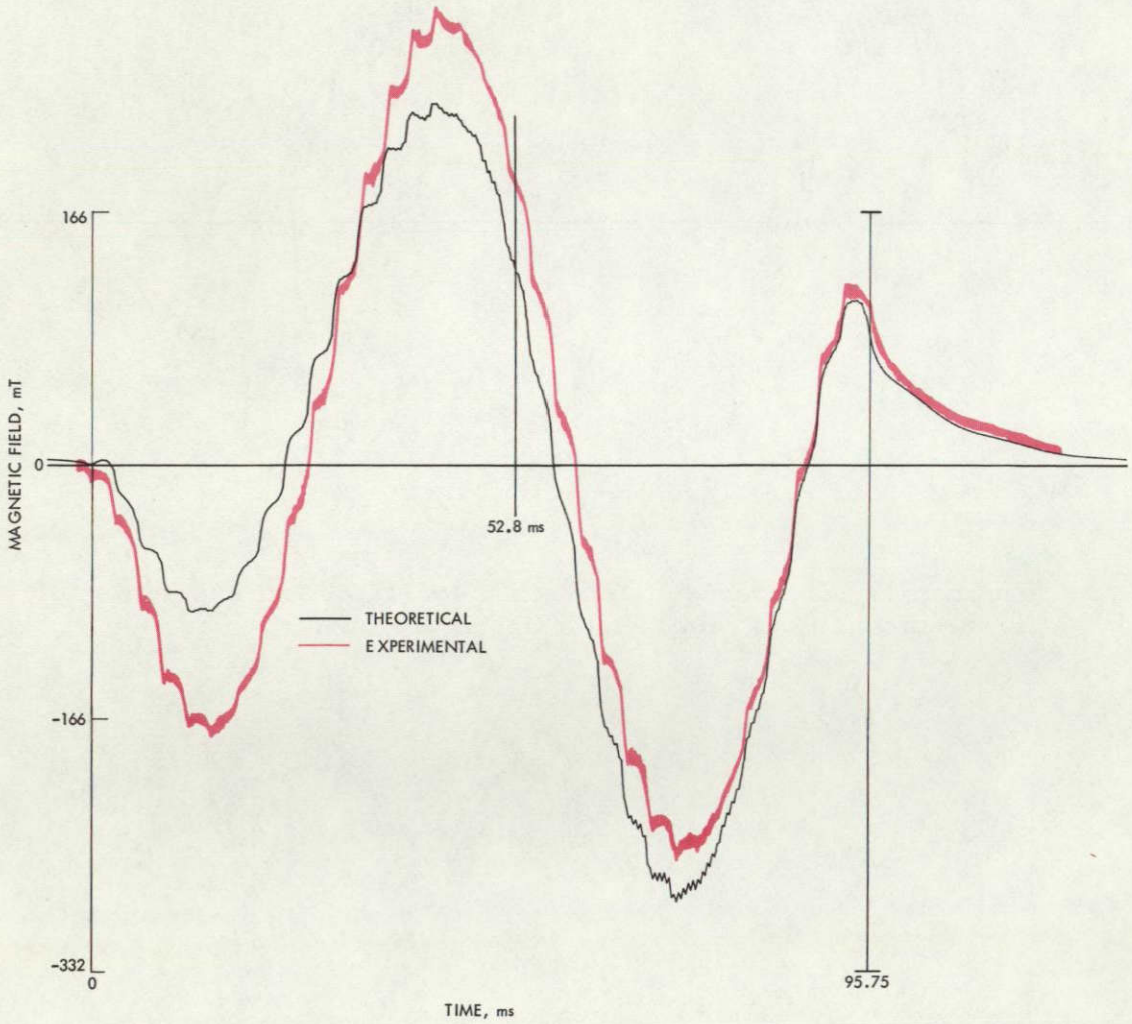

Figure 53. Comparison between theoretical and experimental magnetic fields at sensor F21 in Run 540

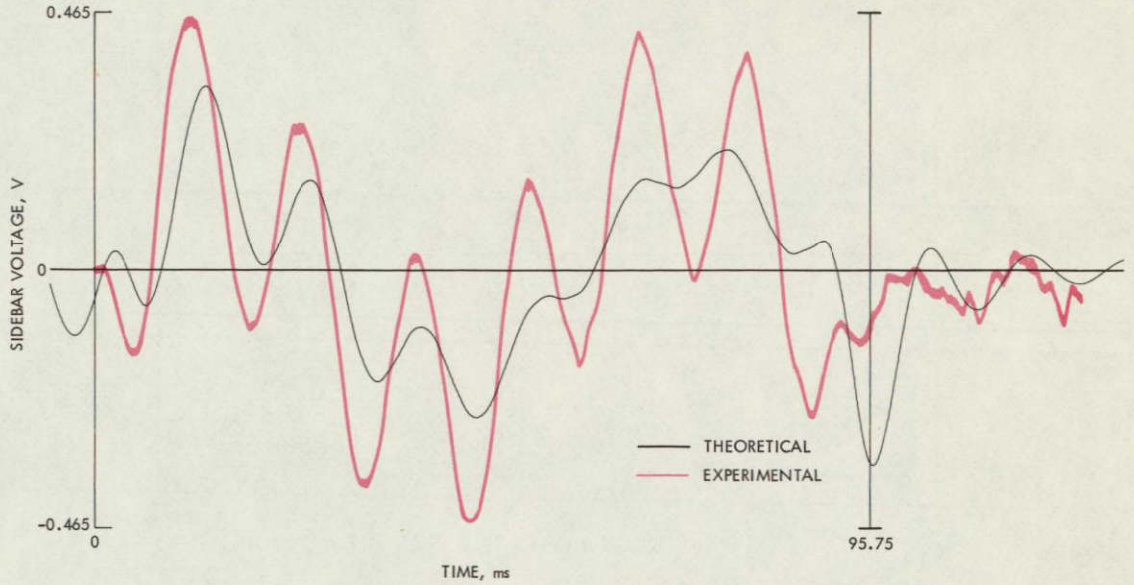

Figure 54. Comparison between theoretical and experimental sidebar voltages at contact SB2 in Run 540

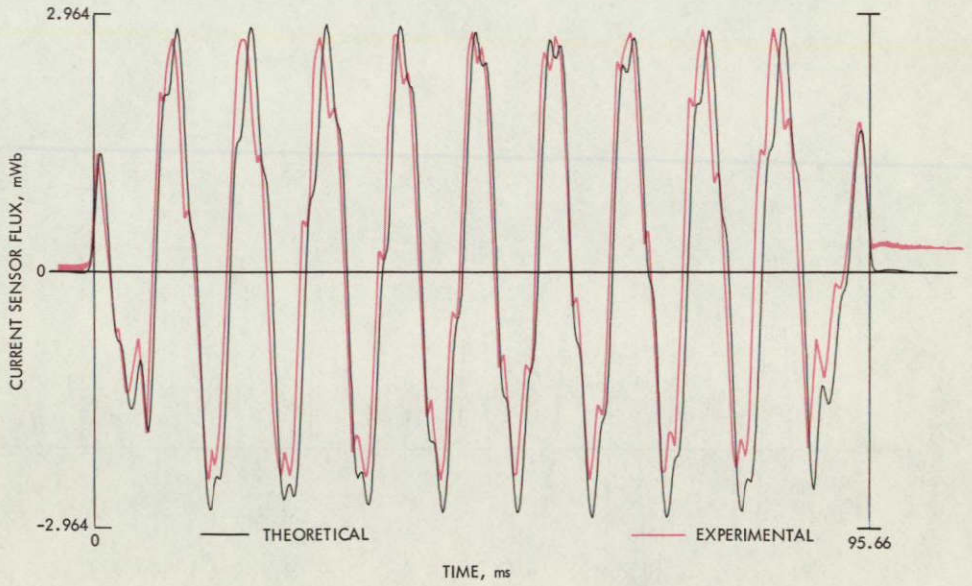

Figure 55. Comparison between theoretical and experimental fluxes through current sensor C22 in Run 544

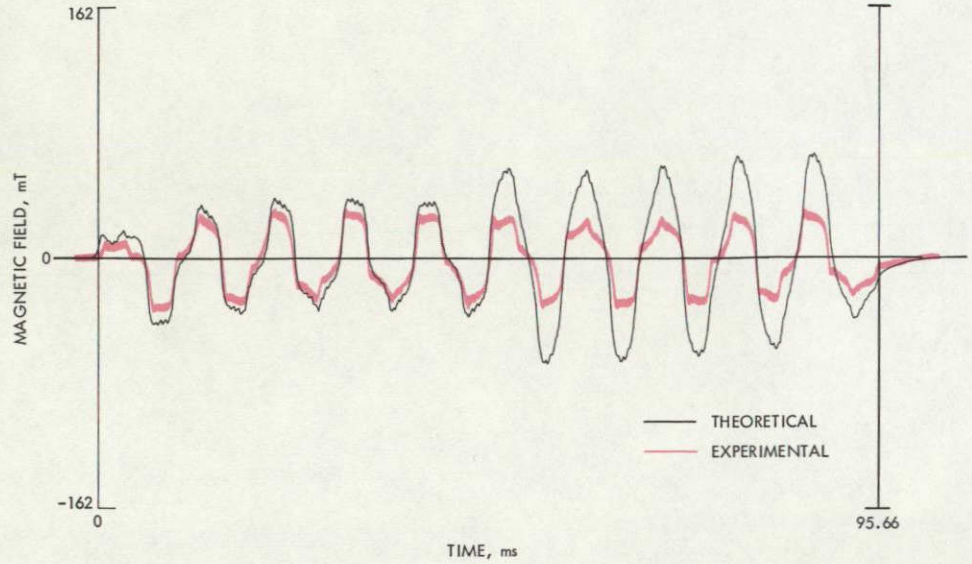

Figure 56. Comparison between theoretical and experimental magnetic fields at sensor F11 in Run 544

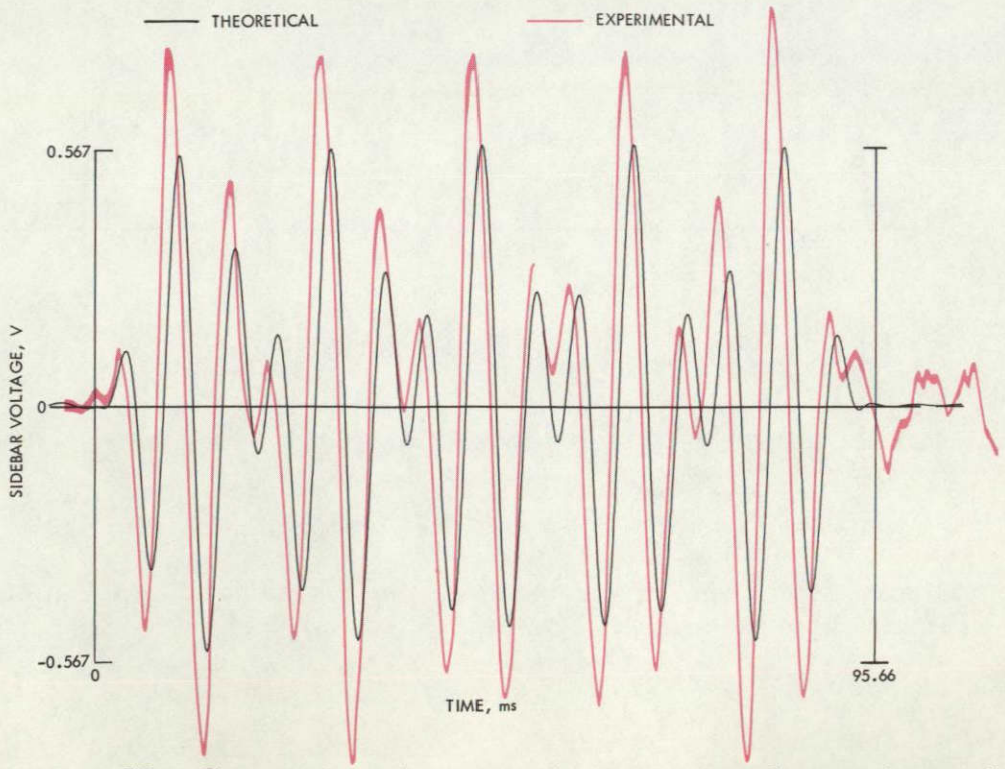

Figure 57. Comparison between theoretical and experimental sidebar voltages at contact SB2 in Run 544

VIII. RECONSTRUCTION OF EXPERIMENTAL PHASORS

It was suggested by R. B. Powell of AiResearch that the pairs of oscillograph records from successive sensing stations can be used to reconstruct the actual phasor quantities in the experimental runs, thus permitting direct comparison between experimental and theoretical amplitudes and phase angles. Figure 58 shows the method of construction. At any given point relative to the motor the observed quantities vary sinusoidally with time. If the field at a particular point in the motor is B and the phase angle of the field when that point is opposite the first sensor coil (sensor F11) is θ, then the output of sensor F11 at that time will be

$$B_1 = |B| \sin \theta \tag{10}$$

If the distance between the first and second sensor stations is Δx, the speed is U, and the angular frequency is ω, the phase shift of the field between the first and second sensor stations is

$$\Delta\theta = \frac{\omega \Delta x}{U} \tag{11}$$

Thus the output of sensor F21, when the same point on the motor reaches the second sensor station, will be

$$B_2 = |B| \sin (\theta + \Delta\theta) \tag{12}$$

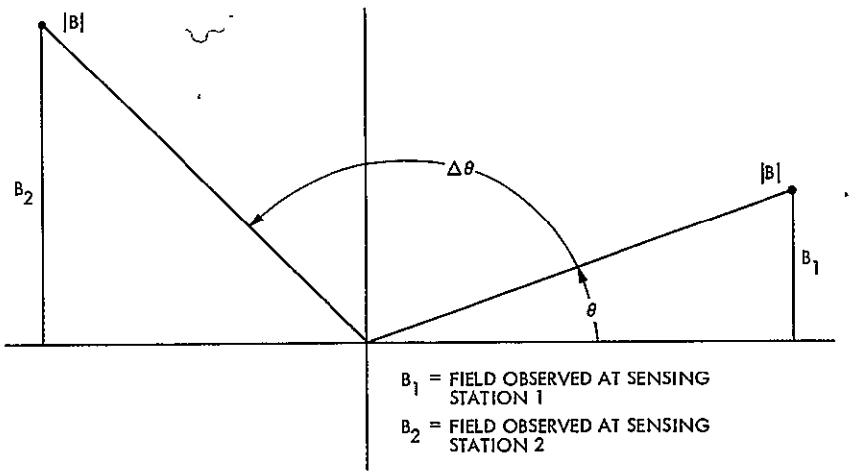

Figure 58. Geometry for reconstruction of phasor from instantaneous values at successive sensing stations

Solving Equations (10) and (12) for θ, the phase angle of the field at station 1 is

$$\theta = \tan^{-1} \frac{\sin \Delta\theta}{\frac{B_2}{B_1} - \cos \Delta\theta} \tag{13}$$

The procedure for reconstructing the phasor field at a given point x along the motor is, therefore, as follows: Measure the deflections B_1 and B_2 of the oscillograph records from sensors F11 and F21 at the time of passage of point x. Calculate $\Delta\theta$ from Equation (11). Find the phase angle at station 1 from Equation (13). Find the field amplitude $|B|$ from Equation (10).

For example, Figure 52 shows that the experimental field at x = 2.1 m from the entrance of the motor (corresponding to time = 2.1/3.81 × 95.75 = 52.8 ms), when that point passes sensor F11, is B_1 = 50 mT. From Figure 53 the experimental field, when the same x-coordinate passes sensor F21, is B_2 = 183 mT. The phase shift between stations from Equation (11), using constants from Table 1 and Figure 2, is $\Delta\theta = (2\pi \times 72.4)(0.1778)/39.79 = 2.033$ rad = 116.5 deg. From Equation (13) the phase angle of the field at x = 2.1 m, when that point reaches sensor F11, is θ = 12.3 deg. From Equation (10) the field amplitude at x = 2.1 m is 235 mT.

If this procedure is repeated for each point x along the motor, and the θ values are all shifted to some arbitrary fixed time, the result is the distribution of the phasor field along the motor. Thus, the two oscillograph records from sensors F11 and F21 contain the complete information on the field in the motor (at the particular sensor height), and not just the instantaneous fields at the particular times of the recording. The same procedure can be used to reconstruct the phasor rail currents.

The experimental phasor fields were reconstructed for Runs 540, 541, and 545. Figure 59 shows the reconstructed field amplitude for Run 541, the run with the largest disagreement between theoretical and experimental thrust (theoretical thrust 26 percent below experimental). The experimental field amplitude rises more rapidly than the theoretical field amplitude, and the

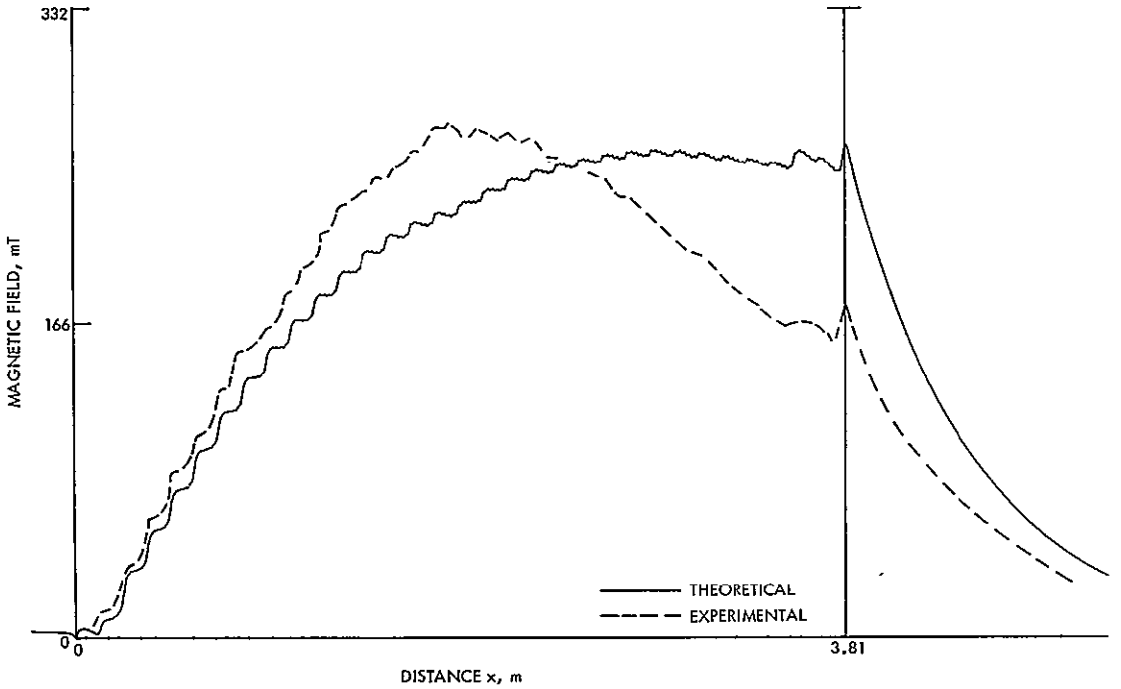

Figure 59. Comparison between theoretical and reconstructed experimental magnetic field amplitude at sensor F11 height in Run 541 (high-speed, low-slip)

experimental field is 20 percent higher than the theoretical field at the center of the motor. But the experimental field then decreases to 60 percent of its peak value, whereas the theoretical field remains constant. The experimental field is only 68 percent of the theoretical field at the exit. Again, these results provide no explanation for the low theoretical thrust prediction.

Figure 60 compares the reconstructed experimental field amplitude with the theoretical field amplitude for Run 545, the run with the largest difference between theoretical and experimental magnetic fields. The experimental field is 60 percent higher than theoretical in the first half of the motor, drops to half the theoretical value in the center, has a second dip not predicted by the theory, and remains at about half of the theoretical field in the last part of the motor.

Figure 61 compares the reconstructed experimental field amplitude with the theoretical field amplitude for Run 540. The differences between the theoretical and experimental fields are similar to those in Run 545, but not as pronounced.

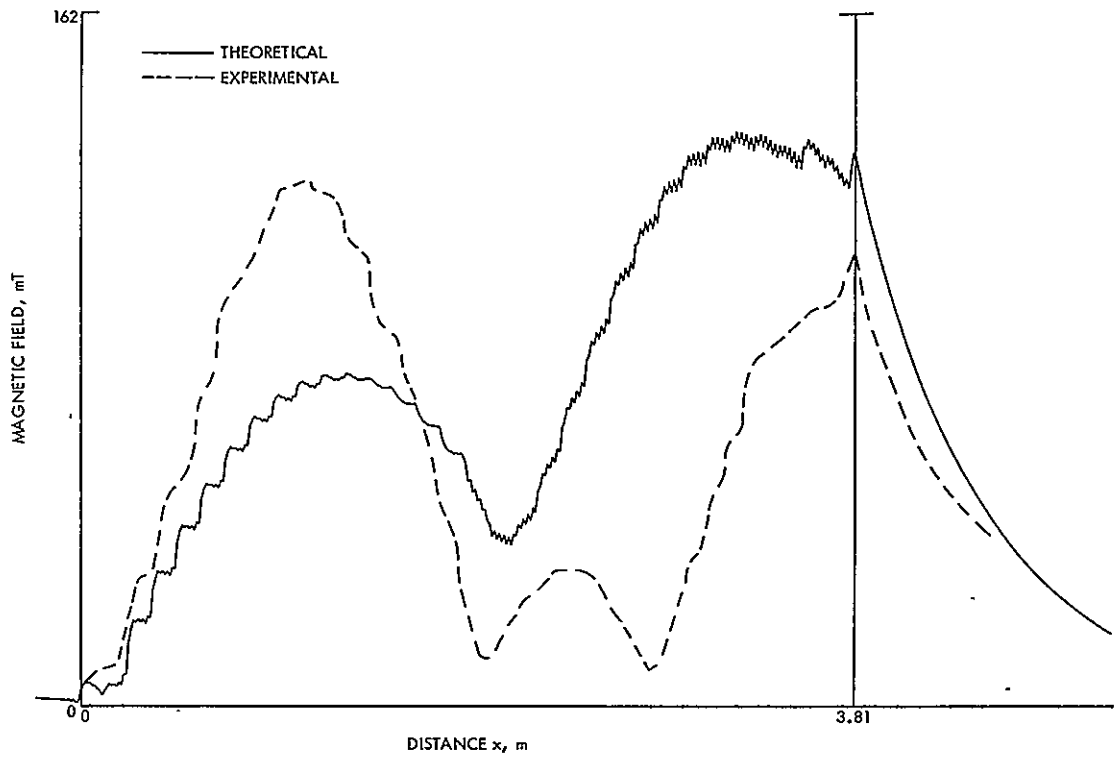

Figure 60. Comparison between theoretical and reconstructed experimental magnetic field amplitude at sensor F11 height in Run 545 (high-speed, medium-slip)

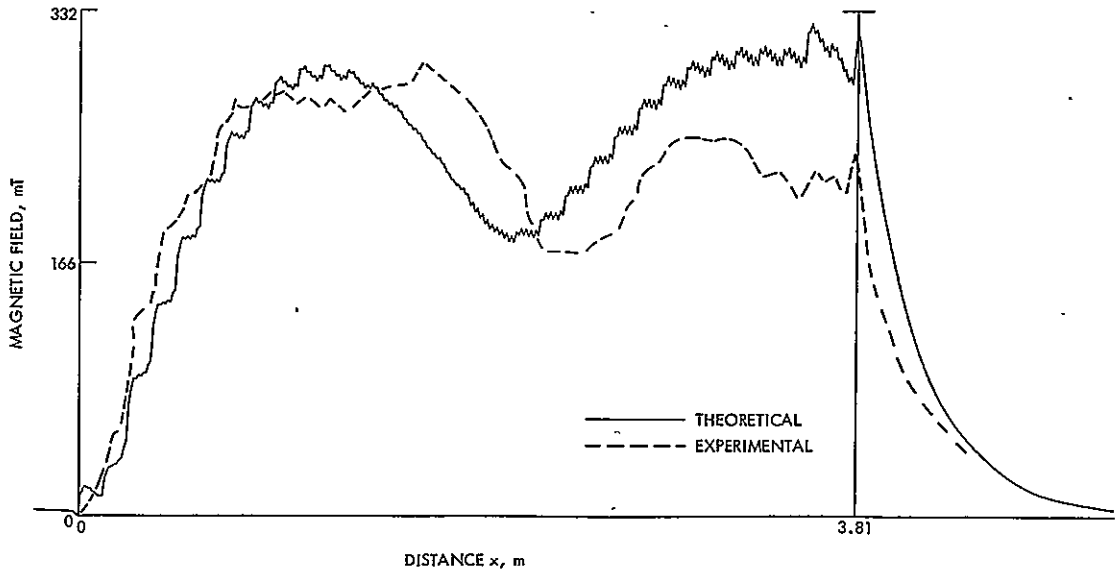

Figure 61. Comparison between theoretical and reconstructed experimental magnetic field amplitude at sensor F11 height in Run 540 (medium-speed, low-slip)

Reconstruction of the phasor quantities would appear to be a superior method of processing the data. The processing could be done by converting the oscillograph recordings to digital form, calculating the phasors from Equations 10)-(13), and machine plotting the results as amplitude and phase angle. This procedure is recommended for future work.

IX. CONCLUSIONS

Based on the comparisons of the theoretical and experimental oscillograph records for the five LIMRV runs considered, the following conclusions are drawn:

(1) The rail currents and magnetic fields predicted by the theory (mesh/matrix combined with Bolton) are within 20 percent of the measured currents and fields at most motor coordinates in most of the runs, but differ by as much as a factor of two at some coordinates in some of the runs.

(2) The most consistent difference between theory and experiment is a higher experimental than theoretical magnetic field near the entrance of the motor and a lower experimental than theoretical magnetic field near the exit.

(3) The observed differences between the theoretical and experimental magnetic fields and currents do not account for the differences between the theoretical and experimental thrusts and powers. A possible source of the higher experimental than theoretical thrust may be a thrust contribution from the fringing field at the sides of the motor.

(4) It is possible to reconstruct the phasor currents and fields from the sensor records at successive stations, and this would permit improved data analysis and comparison with theory in future work.

REFERENCES

1. D'Sena, G. O., and McConville, J. H., LIM Research Vehicle Reaction Rail Current Distribution Tests, Report No. FRA-OR&D-75-18, Federal Railroad Administration, Washington, D. C., Sept. 1973.

2. Powell, R. B., and McConville, J. H., Linear Induction Motor Research Vehicle Reaction Rail Current and Airgap Flux Distribution Test, AiResearch Document No. 75-11965, Federal Railroad Administration, Washington, D. C., Nov. 1975.

3. Bolton, H., "Transverse Edge Effect in Sheet-Rotor Induction Motors," Proc. IEE, Vol. 116, No. 5, pp. 725-731, May, 1969.

4. Bolton, H., "Forces in Induction Motors with Laterally Asymmetric Sheet Secondaries," Proc. IEE, Vol. 117, No. 12, pp. 2241-2248, Dec. 1970.

5. Elliott, D. G., Matrix Analysis of Linear Induction Machines, Report No. FRA-OR&D-75-77, Federal Railroad Administration, Washington, D. C., Sept. 1975.